Coordination of Septate Junctions Assembly and Completion of Cytokinesis in Proliferative Epithelial Tissues

Emeline Daniel, Marion Daude, Irina Kolotuev, Kristi Charish, Vanessa Auld, Roland Le Borgne

Coordination of Septate Junctions Assembly and Completion of Cytokinesis in Proliferative Epithelial Tissues

Emeline Daniel[1]*, Marion Daudé[1]*, Irina Kolotuev[1,2]*, Kristi Charish[3], Vanessa Auld[3] and Roland Le Borgne[1,4,5§]

[1] Univ Rennes, CNRS, IGDR (Institut de Génétique et Développement de Rennes) - UMR 6290, F- 35000 Rennes, France

[2] Present address: EM Facility, Faculté de Biologie et de Médecine, Université de Lausanne, Switzerland

[3] Department of Zoology, Life Sciences Institute, University of British Columbia, Vancouver, Canada;

[4] Équipe Labellisée Ligue Nationale contre le cancer

[5] Lead contact

*** E.D., M.D. and I.K.** have equally contributed to this work

§ Corresponding author: R.L.B.

e-mail: roland.leborgne@univ-rennes1.fr

phone: 33 223 234 894

Running title: Remodeling of septate junctions during cytokinesis

Key words: Epithelial Cells; Cytokinesis; Paracellular Diffusion Barrier; Septate Junctions; Tricellular Junctions; *Drosophila*; Live Imaging, Scanning Face Block Electron Microscopy and Transmission Electron Microscopy

SUMMARY

How permeability barrier function is maintained when epithelial cells divide is largely unknown. Here, we have investigated how the bi (BSJ) and tricellular (TSJ) septate junctions are remodeled throughout completion of cytokinesis in *Drosophila* epithelia. We report that, following cytokinetic ring constriction, the midbody assembles, matures within SJ and is displaced basally in two phases. In a first slow phase, the neighboring cells remain connected to the dividing cells by means of SJ-containing membrane protrusions pointing to the maturing midbody. Fluorescence recovery after photobleaching (FRAP) experiments revealed that SJ present within the membrane protrusions correspond to the old SJ present prior to cytokinesis. In contrast, new SJ are assembled below the adherens junctions and spread basally to build a new belt of SJ, in a manner analogous to a conveyor belt. Loss-of-function of a core BSJ component, the Na/K-ATPase pump Nervana2 subunit, revealed that the apical-to-basal spread of BSJ drives the basal displacement of the midbody. In contrast, loss of the TSJ protein Bark beetle indicated that remodeling of TSJ is rate limiting, and slowed down midbody migration. In the second phase, once the belt of SJ is assembled, the basal displacement of the midbody is accelerated and ultimately leads to abscission. This last step is temporally uncoupled from the remodeling of SJ. We propose that cytokinesis in epithelia involves the coordinated polarized assembly and remodeling of SJ both in the dividing cell and its neighbors to ensure the maintenance of permeability barrier integrity in proliferative epithelia.

INTRODUCTION

Epithelia serve as mechanical and chemical barriers essential for the function of all organs. Adherens junctions (AJ) form the mechanical barrier [1], while tight (TJ)/septate (SJ) junctions create the permeability barrier, in vertebrates and invertebrates respectively [2-5]. Throughout life, epithelia are continuously growing, undergoing morphogenesis or regenerating in part due to cell division. Common to each division is the generation of a new cell-membrane interface and two cell vertices. These cell shape changes imply junctional plasticity with major disassembly and *de novo* assembly of junctions. However, AJ and TJ/SJ are composed of protein complexes exhibiting different rates of assembly/disassembly ranging from time scales of minutes for AJ, to tens of minutes or hours for TJ/SJ [6-11]. Previous work revealed that formation of the new adhesive interface is coordinated with cytokinesis and the strength of adhesion with neighbors impacts both the kinetics of AJ remodeling and the geometry of the new AJ [7, 12-17]. AJ determine the positioning of the midbody immediately basal to the forming AJ in invertebrates [12-15], or apical to AJ in vertebrates [7, 18, 19]. Similar to the mechanical barrier, permeability barrier must be preserved throughout cytokinesis. How permeability barrier maintenance is coordinated with cytokinetic abscission during epithelial division remains largely unexplored.

Cytokinesis starts at the onset of anaphase when the spindle drives the assembly of an actomyosin ring that constricts and draws in the cell membrane [20, 21]. After constriction the spindle and the actomyosin ring form the midbody and the midbody ring, which eventually directs the physical separation of daughter cells, i.e. the abscission [22, 23]. The midbody ring retains components of the actomyosin contractile ring including actin and septin, non-muscle Myosin II, and Anillin [24]. The midbody consists in a densely packed array of antiparallel microtubules containing among others the chromosomal passenger complex (CPC), and eventually recruits the endosomal sorting complex (ESCRT-III) to allow for membrane remodeling during membrane constriction and fission [23, 25-28]. Whether these fundamental mechanisms extensively described in isolated cells [20, 21] apply to epithelia remains unknown. In addition, because epithelial cytokinesis is a multicellular process, whether junctional complexes exert a role during midbody maturation is also unknown.

TJ/SJ seal the intercellular space between adjacent cells forming a physical barrier restricting paracellular flux and preventing pathogens from crossing epithelia [3]. In *Drosophila*, SJ are characterized by septae, ladder-like rungs that span between adjacent cells [2]. The bicellular

septate junctions (BSJ) are made of a large protein complex comprising more than thirteen proteins [4, 29, 30], with a core complex that includes Neurexin IV (Nrx-IV), Coracle (Cora), Neuroglian (Nrg), and the α- and β-subunits of the Na^+/K^+ ATPase pump (ATPα and Nervana 2 (Nrv2)) [31-34]. At three-cell vertices, BSJ are disjointed and specialized tricellular junctions (TSJ) mediate cell contacts [35-39]. *Drosophila* TSJ contains the Neuroligin-like transmembrane protein Gliotactin (Gli) [39], which is recruited by the triple-extracellular repeat protein Bark beetle (Bark, a.k.a. Anakonda) [38, 40]. It is currently unknown how, when and where SJ components are recruited and stabilized to assemble *de novo* BSJ and TSJ to ensure maintenance of permeability barrier function throughout cytokinesis.

Here, we analyzed the maturation of the midbody and the remodeling of SJ upon cell division in the *Drosophila* pupal notum and larval wing imaginal disc (WID) epithelia (Figure S1). They are composed of cuboidal and columnar epithelial cells respectively, undergo numerous cell divisions, can be subjected to *in vivo* quantitative live imaging and to genetic dissection. We identified how new BSJ and TSJ are remodeled as the midbody matures to ensure the *de novo* permeability barrier maintenance in proliferative epithelia.

RESULTS

Maturation and basal displacement of the midbody during epithelial cytokinesis

To explore cytokinesis, we imaged the actomyosin contractile ring using the non-muscle Myosin II light chain tagged with RFP or mCherry (thereafter referred to as MyoII::RFP) together with the AJ marker E-Cadherin (E-Cad)::GFP or the SJ marker ATPα::YFP using time-lapse confocal microscopy on the notum (Figures 1A-B).

Upon completion of constriction, the actomyosin ring was located below the newly formed adhesive interface (Figure 1A; Movie S1), as previously described [12-15]. MyoII::RFP remained associated with and marked the midbody ring (Figure 1A-B). The midbody moved towards the basal pole over two main phases. In the first, slow phase, the midbody moved ~3 µm within the SJ domain (Figures 1B,C, andS2A). In the second phase, upon exit from the SJ domain, the midbody moved faster basally (from t=1h30min, Figure 1B,C,).

By analogy to isolated cells [20, 21], the composition and the morphology of the midbody should evolve as it matures into an intercellular bridge. This prediction was by imaging midbody

components. For each marker, any drift was corrected to artificially immobilize the midbody, allowing us to represent the changes in composition in the form of kymographs. We found that MyoII, Septin 2 (Sep2) and Septin 7 (a.k.a. Peanut (Pnut)), remained localized to the midbody ring for more than 120 minutes after the onset of anaphase (Figure 1D). FRAP experiments revealed that MyoII::RFP and Pnut::mCherry remained stably associated within the midbody (Figures 1E-F, S2B-C, Movies S3 and S4). In contrast, actin visualized using LifeAct::mCherry and microtubules visualized with Jupiter::GFP were no longer detected in the midbody at t=26 ± 4 min and t=42 ± 6 min respectively after the onset of anaphase (Figure 1D; Movie S2).

We next confirmed these data, using transmission- (TEM) and serial block face scanning- (SFB-SEM) electron microscopy [41] in the notum (Figure 1G-M; Movie S5) and WID (Figure S2D-G). The maturing midbody was characterized by the presence of an array of microtubules (Figures 1G-H and S2D; Movie S6) predominantly found in the apical side of dividing cells (Figures 1L-M and S2G, magenta). At an intermediate stage, most of microtubules disappeared and were replaced by internal membranes (Figures 1I, L-M, green, and S2E; Movie S7), until the maturation into intercellular bridges that were found more basally (Figures 1J,L-M and S2F,G, Cyan; Movie S8).

These data indicate that basal displacement and maturation of the midbody is conserved in the notum and WID, raising the question of when and where completion of cytokinesis occurs.

Epithelial cell abscission

TEM of the WID revealed that intercellular bridges were ultimately detected in intracellular compartments (Figures 2A and S3A), presumably resulting from internalization. Such bridges followed an asymmetric pattern with one side opened to the cytosol and the other side sealed by membrane as a result of abscission (Figure 2A). The internalized bridges were eventually degraded (Figures 2B and S3B-E) and most were localized in the basal side (Figure S3F).

To monitor the timing of abscission in the notum, we found that CPC components Aurora B (AurB) and Survivin (Svv) left the midbody concomitantly with microtubules (Figures 1D and 2C; AurB::GFP: t=45 ± 7 min; Svv::GFP: t=40 ± 5 min). The ESCRT-III component Shrub::GFP (Shrb, the Chmp4B ortholog) was recruited at the midbody at t=22 ± 8 min following the onset of anaphase (Figure 2C), suggesting that cells are set for abscission ~40 minutes post-anaphase onset. As an independent measure of abscission, we analyzed cytoplasmic isolation of the two daughter cells [25, 42, 43] using the photoconvertible KAEDE. Photoconverted KAEDE can

freely diffuse between daughter cells through the intercellular bridge prior to cytoplasmic isolation, and diffusion will cease upon abscission (Figure S3G-H**).** When KAEDE was photoconverted in one daughter cell, we found that even 5 hours after the onset of anaphase, cytoplasmic isolation had not yet occurred (Figure 2D). These data demonstrate that recruitment of Shrb to the midbody and cytoplasmic isolation occur at distinct times.

Given the time lag between midbody maturation and abscission, and the two phases of midbody displacement, the question arises as to what forces are driving midbody basal displacement? Because it occurred within the SJ, we asked how SJ are remodeled during cytokinesis and could contribute to midbody displacement.

Connection between dividing cells and their neighbors during cytokinesis

To monitor SJ remodeling, we imaged MyoII::RFP together with ATPα::YFP in the notum. We observed that the neighboring interphase cells make membrane protrusions that pointed towards the midbody, hereafter called finger-like protrusions (Figure 3A). Such protrusions labeled with Nrg::GFP were also observed in the WID (Figure S4A,B) suggesting this is a common feature of *Drosophila* epithelial cytokinesis.

To unambiguously establish that neighbors retain contact with dividing cells, we generated clones devoid of ATPα::YFP in a tissue expressing ATPα::YFP and MyoII::RFP. When a YFP-negative cell (Figure 3B) divided next to an ATPα::YFP-positive cell, the YFP signal exclusively originated from the neighboring cell. The latter remained connected with the mitotic cell at the level of the midbody where membrane deformation was maximal due to cytokinetic ingression (Figure 3C). At the time the new AJ were already assembled (Figure 3C, t=10 min), the finger-like protrusions containing ATPα::YFP were already present and persisted for more than 2h30.

3D modeling of a SEM dataset further demonstrated the presence of finger-like protrusions at the level of the midbody in the notum as well as in WID (Figures 3D-H and S4C-D). TEM revealed that dividing cells form a tight, four-cell contact with their neighbors at the level of the midbody (Figure 3I-K). As the midbody matured, these finger-like protrusions were displaced towards the basal pole (Figure 3C). The maintenance of finger-like protrusions through the basal displacement suggests that these contacts have biological significance in dividing epithelia.

***De novo* assembly of SJ at the cleavage site**

During cytokinesis, new BSJ will assemble along the interface between daughter cells. Meanwhile, at the cleavage site, the dividing cells need to disassemble and remodel the prior SJ to create a TSJ at the newly formed cell corners.

To monitor BSJ assembly, we imaged clones of dividing cells expressing ATPα::YFP surrounded by interphase cells devoid of ATPα::YFP (Figures 4A and S5A). The new BSJ, marked by the only source of ATPα::YFP in the dividing cell, were found to assemble apical to the midbody (Figure 4A). As the midbody was displaced basally, BSJ continued to assemble culminating in the formation of the characteristic belt of BSJ seen in interphase cells (Figure 4A, t=1h20). It was at this point the intercellular bridge moved toward the basal side with faster kinetics.

To monitor TSJ remodeling, we imaged Gli::YFP, which was detected apical to the midbody (Figure 4B). In contrast to ATPα::YFP, which was uniformly recruited along the new membrane interface, Gli::YFP appeared first as a single puncta (Figure 4B, t=23 min), which expanded to two (t=33 min), three (t=38 min) where the addition of subsequent punctae yielded the appearance of a pearl necklace (t=1h23) along the finger-like protrusions. Between t=1h23 and t=2h33, the pearl-like distribution was no longer detected, and Gli::YFP was exclusively detected at the three-cell corners. It was after this stage the intercellular bridge was displaced faster basally (Figure 4B, red arrows at t=2h23 to t=2h33). Bark::GFP, which recruits and stabilizes Gli at TSJ [38], exhibited comparable spatio-temporal localization than Gli::YFP throughout cytokinesis (Figure S5B).

Overall our findings suggest that BSJ assembly during cytokinesis is an inherently slow process and the completion of SJ assembly is linked to the different phases of midbody displacement.

Slow and polarized SJ assembly along the apico-basal axis

BSJ are highly stable in *Drosophila* embryos [6] and thus the duration of SJ remodeling during cytokinesis could be limited by slow junctional turnover. We tested this possibility using FRAP and found that most of ATPα::YFP was found in an immobile fraction in mitotic cells. About 90 minutes were required to recover ~80% of ATPα::YFP fluorescence, confirming a stable protein complex (Figure 5A, D, G). The kinetics of fluorescence recovery of ATPα::YFP in interphase cells (Figure 5B, E, H) was only slightly faster (ANOVA, p-value=0.019 *, Figure 5A, D, G) indicating that SJ renewal is largely cell-cycle independent. Similar to ATPα::YFP, Bark was

stable at the TSJ as ~80% of Bark::GFP signal was recovered in 90 minutes in interphase cells (Figure 5C, F, I).

FRAP experiments revealed that the recovery of fluorescence was polarized. The recovery of ATPα::YFP fluorescence occurred first apically, 1 µm below the AJ, in mitotic and interphase cells (Figure 5D-E, G-H, black frames). At 2 µm below the AJ, recovery occurred later (Figure 5E, H, blue frame) (ANOVA, p-value<$2.2x10^{-16}$ ***). Bark recovery was also polarized along the apical basal axis (Figure 5F, I).

Very little or no ATPα::YFP signal was recovered in the finger-like protrusions formed by the neighboring interphase cells (Figure 5D, G, red frame). These BSJ likely correspond to the prior SJ present before mitosis.

Collectively, these data show that BSJ and TSJ are assembled apically, and spread from the apical to basal side as they age, in a manner akin to a conveyor belt.

Coordination between assembly of SJ and basal displacement of the midbody

The above findings raise the possibility that assembly of BSJ and TSJ regulate the basal displacement of the finger-like protrusions connected to the midbody. To test this prediction, we analyzed the kinetics of the midbody basal displacement upon loss of BSJ or TSJ components.

Depletion of the core BSJ components Nrx-IV and Cora, disrupted cell polarity leading to cell delamination and prevented further analyses (data not shown). We found that loss of the core component Nrv2, impaired SJ integrity as judged by the strong reduction in ATPα::YFP, Fas3, Gli and Cora staining without affecting E-Cad localization (Figures 6A-B and S6A-C). FRAP analyses in *nrv2*^{k13315} mutant cells indicated that the remaining ATPα::YFP resided mostly in a mobile fraction with ~80% recovery and $t_{1/2}$=30 ± 6 sec (Figures 6C and S6H, K). This is in striking contrast to controls where ~19% of ATPα::YFP was in a mobile fraction ($t_{1/2}$=28 ± 6 sec) (Figures 6C and S6G, J) and the bulk of ATPα::YFP in an immobile fraction (Figure 5H). In contrast to the percentage of recovery (t-test, p-value=$1.26x10^{-14}$ ***), the halftimes are not significantly different (t-test, p-value=0.28) between wild-type and *nrv2*^{k13315} mutant cells. These data suggest that the assembly of ATPα::YFP-containing junctions were impaired upon loss of Nrv2. Only the mobile fraction remained, which displayed rapid recovery. Furthermore, the finger-like protrusions were no longer detected in *nrv2*^{k13315} mutant cells (Figure 6B), even within wild-type cells dividing next to *nrv2*^{k13315} mutant cells (Figure 6A). Finally, the midbody was not displaced basally in *nrv2*^{k13315} mutant cells over time compared to wild-type cells (Figure 6D,E,

ANCOVA, p-value<$2.2x10^{-16}$ ***). Collectively, these data suggest that polarized assembly of BSJ drives midbody basal displacement.

To test whether TSJ influence midbody basal displacement, we analyzed the consequence of loss of Bark [38]. While dispensable for E-Cad localization, as expected, Bark was needed to recruit Gli [38] (Figure S6E). Loss of Bark also disrupted the BSJ, where ATPα::YFP, Fas3 and Cora staining was reduced and spread basally (Figures 6F-G and S6D, F), and membrane deformations were observed (Figure S6F, white inset). Despite these morphological changes, loss of Bark did not modified the stability of ATPα::YFP as measured by FRAP (Figures 6H and S6I, L) (ANOVA, p-value=0.62). In contrast to Nrv2, loss of Bark did not modify the assembly or the stability of BSJ complexes, and loss of Bark did not impair the finger-like protrusions with neighboring cells at cytokinesis (Figure 6F-G). Also in contrast to Nrv2, the basal displacement of the midbody was accelerated in *bark*^{L200} mutant cells (Figure 6I-J; ANCOVA, p-value<$2.2x10^{-16}$ ***), indicating that the remodeling of TSJ is rate-limiting, slowing down the midbody basal displacement.

Based on these data, we propose a model where the remodeling of SJ and TSJ between dividing cells and their neighbors regulates the kinetics of midbody basal displacement (Figure 7).

DISCUSSION

Coordination between SJ remodeling and basal displacement of the midbody

Epithelial growth requires the formation of cell-cell junctions and physical separation of daughters upon cell division. Here, in both cuboidal and columnar epithelia we have characterized a multicellular mechanism that coordinates completion of cytokinesis and *de novo* formation of SJ (Figure 7): 1) Following actomyosin ring constriction, the midbody forms just basal to the AJ within the SJ and matures into an intercellular bridge that is displaced basally. 2) Neighboring interphase cells maintain SJ contacts, the finger-like protrusions connecting to the maturing midbody of the dividing cells. At this position, the *ménage à quatre* formed contains preexisting SJ and is stable. 3) Novel BSJ are assembled below the AJ and above the finger-like protrusions and spread towards the basal side, thereby driving the basal displacement of the finger-like protrusion plus midbody. Once the new BSJ is complete the midbody is positioned outside the SJ belt and basal displacement accelerated. Overall, we propose that this

multicellular process is to ensure the maintenance of the permeability barrier throughout cytokinesis.

Role of polarized delivery and assembly of BSJ in midbody basal displacement

Our data show that, as in embryos [6], newly synthesized SJ components assemble into stable protein complexes exhibiting a low rate of diffusion, endocytosis and recycling. These stable complexes assemble below the AJ and then propagate towards the basal pole, in a manner analogous to a conveyor belt, both in interphase and during cytokinesis.

Loss of the core SJ component Nrv2 prevents both assembly of stable BSJ complexes and basal displacement of the midbody. Thus, we propose that the apico-basal flux of newly assembled BSJ is the propelling force for the basal displacement of the finger-like protrusions connected to the midbody. The conveyor belt model first predicts that newly synthesized and/or slowly recycling SJ components are delivered apically in the vicinity of AJ. The model also predicts that SJ disassembly occurs at the basal rim of SJ belt. Future work will determine what regulates the polarized traffic of SJ components and the disassembly of SJ to control both the positioning and thickness of the SJ belt.

Site of TSJ assembly and role in midbody displacement

Our study sheds light on the remodeling of TSJ at cytokinesis. Bark and Gli are initially detected as puncta next to the midbody, prior to the pearl necklace distribution along the finger-like protrusions. These dotted structures could represent new TSJ, as at this location a new three-way contact is formed between the two daughter cells and a neighbor. However, FRAP analyses suggest that these punctae do not contain exchangeable components and are not moving laterally (our unpublished results). Moreover, the appearing of Gli and Bark punctae in mitotic cells is faster (20 min post-anaphase) than the *de novo* assembly of TSJ in interphase cells (~80% recovery in 90 min). Analyses of the punctae by TEM will be necessary to test if they are *bona fide* TSJ or components in the process of assembly. Alternatively, the old TSJ between dividing cells and neighbors prior to mitosis could undergo a change in distribution from a uniform distribution into clusters giving rise to the pearl necklace. Redistribution could represent an intermediate step in TSJ disassembly and may explain the fast kinetics of assembly of pearl necklace structure. Future work using for example photoconvertible probes would help address this issue.

Finally, loss of Bark resulted in acceleration of the midbody basal displacement. The *de novo* assembly of TSJ in the pearl necklace structure could be the rate-limiting step that imposes the slower speed of basal displacement. Alternatively, if pearl necklace represents the remodeling of prior TSJ connections with neighboring cells, TSJ disassembly maybe the rate-limiting step.

Regardless, our data argue that the TSJ components present in the pearl necklace slow down the midbody basal displacement driven by the BSJ mediated conveyor belt.

Completion of epithelial cytokinesis

Our study reveals differences in midbody maturation and organization of the intercellular bridge between isolated and epithelial cells. In epithelial cells, the densely packed microtubule array that normally sits in the center of the intercellular bridge and the Flemming body were not observed [44]. Instead, we found an intercellular bridge with a uniform density of microtubules that progressively disappear. The electron dense material detected along the plasma membrane of the intercellular bridge could act as a rigid scaffold preventing membrane constriction. The SJ core components, plus MyoII and Pnut at the interface made between the intercellular bridge and the finger-like protrusions might be part of the electron dense material and therefore contribute to membrane rigidity. Alternatively, this scaffold could prevent tension release within the intercellular bridge, therefore preventing premature abscission [45].

We also found that abscission is asymmetric with the bridge remnant internalized and then degraded in one of the daughter cells in a mode similar to the internalization and autophagy described for isolated cells [46]. However, we cannot exclude that abscission could also occur on both side of the bridge leading to its release followed by its recapture by endocytosis in some epithelial cells [23, 46-49].

Finally, while epithelial cells seem to be set for abscission about 40 minutes following the onset of anaphase, cytoplasmic isolation had not occurred 5 hours later. Photoconversion data furthermore suggests that cytoplasmic isolation takes place about one hour prior to one of the sister entering mitosis (Figure S3H), possibly at the mid- to late G2 phase as reported for germline stem cells [27].

Conservation in vertebrates?

Despite the opposite apico-basal positioning of permeability barrier relative to the mechanical barrier, a number of similarities are encountered in vertebrates and invertebrates epithelial cells. First, mechanical barrier transmission during epithelial cytokinesis is a multicellular process [7, 12-17]. Second, the permeability barrier is also maintained throughout epithelial cytokinesis [7]. Third, is the recruitment of tricellular junction components in close vicinity to the midbody, supporting the idea that polarized delivery, membrane composition and topology at midbody is engineered for tricellular junction remodeling. Fourth, epithelial cytokinesis is polarized along the apico-basal axis leading to the embedding of midbody *en route* to abscission within the permeability barrier both in vertebrates [7, 18, 19] and in *Drosophila* (this study). Based on our findings, we anticipate that the coordination between permeability barrier transmission and completion of cytokinesis in *Drosophila* is conserved in vertebrates for maintenance of tissue integrity in proliferative epithelia.

ACKNOWLEDGMENTS

We thank S. Luschnig, R. Karess, F. Payre, the Bloomington Drosophila Stock Center, the Drosophila Genetic Resource Center, the National Institute of Genetics Fly Stock Center, and the Developmental Studies Hybridoma Bank, for providing fly stocks, antibodies.

We also thank the Microscopy Rennes Imaging Center-BIOSIT facility; Y. Le Cunff for statistical analyses and T. Garber for 3D modeling; and T. Starborg from the EM facility of the University of Manchester (U.K.). We thank A. Pacquelet and members of R.L.B.'s laboratory for critical reading of the manuscript.

This work was supported by the Ministère de la Recherche (E.D. and M.D.), the Canadian Institutes of Health Research (V.A.), the Ligue Nationale contre le Cancer-Equipe Labellisée (EL2014-LNCC to R.L.B.), the Fondation ARC contre le Cancer (PJA20151203510 to R.L.B.) and the ANR (ANR-16-CE13-004-01 to R.L.B.).

AUTHOR CONTRIBUTIONS

Conceptualization, E.D., I.K., V.A. and R.L.B.; Methodology, E.D., M.D., I.K., and K.C.; Investigation, E.D., M.D., I.K. and K.C.; Formal Analysis, E.D. and M.D.; Visualization, E.D. and I.K.; Writing-Original Draft, R.L.B.; Writing-Review & Editing, E.D., M.D., I.K., V.A. and R.L.B.; Funding Acquisition, V.A. and R.L.B.; Supervision, E.D., V.A. and R.L.B.

Declaration of Interests

The authors declare no competing interests.

REFERENCES

1. Harris, T.J., and Tepass, U. (2010). Adherens junctions: from molecules to morphogenesis. Nature reviews. Molecular cell biology *11*, 502-514.
2. Tepass, U., Tanentzapf, G., Ward, R., and Fehon, R. (2001). Epithelial cell polarity and cell junctions in Drosophila. Annu Rev Genet *35*, 747-784.
3. Shin, K., Fogg, V.C., and Margolis, B. (2006). Tight junctions and cell polarity. Annual review of cell and developmental biology *22*, 207-235.
4. Banerjee, S., Sousa, A.D., and Bhat, M.A. (2006). Organization and function of septate junctions: an evolutionary perspective. Cell Biochem Biophys *46*, 65-77.
5. Tsukita, S., Furuse, M., and Itoh, M. (2001). Multifunctional strands in tight junctions. Nature reviews. Molecular cell biology *2*, 285-293.
6. Oshima, K., and Fehon, R.G. (2011). Analysis of protein dynamics within the septate junction reveals a highly stable core protein complex that does not include the basolateral polarity protein Discs large. Journal of cell science *124*, 2861-2871.
7. Higashi, T., Arnold, T.R., Stephenson, R.E., Dinshaw, K.M., and Miller, A.L. (2016). Maintenance of the Epithelial Barrier and Remodeling of Cell-Cell Junctions during Cytokinesis. Current biology : CB *26*, 1829-1842.
8. Levayer, R., Pelissier-Monier, A., and Lecuit, T. (2011). Spatial regulation of Dia and Myosin-II by RhoGEF2 controls initiation of E-cadherin endocytosis during epithelial morphogenesis. Nature cell biology *13*, 529-540.
9. Shen, L., Weber, C.R., and Turner, J.R. (2008). The tight junction protein complex undergoes rapid and continuous molecular remodeling at steady state. The Journal of cell biology *181*, 683-695.
10. Yamada, S., Pokutta, S., Drees, F., Weis, W.I., and Nelson, W.J. (2005). Deconstructing the cadherin-catenin-actin complex. Cell *123*, 889-901.
11. Huang, J., Huang, L., Chen, Y.J., Austin, E., Devor, C.E., Roegiers, F., and Hong, Y. (2011). Differential regulation of adherens junction dynamics during apical-basal polarization. Journal of cell science *124*, 4001-4013.
12. Herszterg, S., Leibfried, A., Bosveld, F., Martin, C., and Bellaiche, Y. (2013). Interplay between the dividing cell and its neighbors regulates adherens junction formation during cytokinesis in epithelial tissue. Developmental cell *24*, 256-270.
13. Founounou, N., Loyer, N., and Le Borgne, R. (2013). Septins regulate the contractility of the actomyosin ring to enable adherens junction remodeling during cytokinesis of epithelial cells. Developmental cell *24*, 242-255.
14. Guillot, C., and Lecuit, T. (2013). Adhesion disengagement uncouples intrinsic and extrinsic forces to drive cytokinesis in epithelial tissues. Developmental cell *24*, 227-241.
15. Morais-de-Sa, E., and Sunkel, C. (2013). Adherens junctions determine the apical position of the midbody during follicular epithelial cell division. EMBO reports *14*, 696-703.
16. Lau, K., Tao, H., Liu, H., Wen, J., Sturgeon, K., Sorfazlian, N., Lazic, S., Burrows, J.T., Wong, M.D., Li, D., et al. (2015). Anisotropic stress orients remodelling of mammalian limb bud ectoderm. Nature cell biology *17*, 569-579.
17. Firmino, J., Rocancourt, D., Saadaoui, M., Moreau, C., and Gros, J. (2016). Cell Division Drives Epithelial Cell Rearrangements during Gastrulation in Chick. Developmental cell *36*, 249-261.
18. Jinguji, Y., and Ishikawa, H. (1992). Electron microscopic observations on the maintenance of the tight junction during cell division in the epithelium of the mouse small intestine. Cell structure and function *17*, 27-37.

19. Dubreuil, V., Marzesco, A.M., Corbeil, D., Huttner, W.B., and Wilsch-Brauninger, M. (2007). Midbody and primary cilium of neural progenitors release extracellular membrane particles enriched in the stem cell marker prominin-1. The Journal of cell biology *176*, 483-495.
20. Green, R.A., Paluch, E., and Oegema, K. (2012). Cytokinesis in Animal Cells. Annual review of cell and developmental biology.
21. Glotzer, M. (2005). The molecular requirements for cytokinesis. Science *307*, 1735-1739.
22. Fededa, J.P., and Gerlich, D.W. (2012). Molecular control of animal cell cytokinesis. Nature cell biology *14*, 440-447.
23. Agromayor, M., and Martin-Serrano, J. (2013). Knowing when to cut and run: mechanisms that control cytokinetic abscission. Trends in cell biology.
24. Kechad, A., Jananji, S., Ruella, Y., and Hickson, G.R. (2012). Anillin acts as a bifunctional linker coordinating midbody ring biogenesis during cytokinesis. Current biology : CB *22*, 197-203.
25. Guizetti, J., Schermelleh, L., Mantler, J., Maar, S., Poser, I., Leonhardt, H., Muller-Reichert, T., and Gerlich, D.W. (2011). Cortical constriction during abscission involves helices of ESCRT-III-dependent filaments. Science *331*, 1616-1620.
26. Eikenes, A.H., Malerod, L., Christensen, A.L., Steen, C.B., Mathieu, J., Nezis, I.P., Liestol, K., Huynh, J.R., Stenmark, H., and Haglund, K. (2015). ALIX and ESCRT-III coordinately control cytokinetic abscission during germline stem cell division in vivo. PLoS genetics *11*, e1004904.
27. Matias, N.R., Mathieu, J., and Huynh, J.R. (2015). Abscission is regulated by the ESCRT-III protein shrub in Drosophila germline stem cells. PLoS genetics *11*, e1004653.
28. Mierzwa, B.E., Chiaruttini, N., Redondo-Morata, L., von Filseck, J.M., Konig, J., Larios, J., Poser, I., Muller-Reichert, T., Scheuring, S., Roux, A., et al. (2017). Dynamic subunit turnover in ESCRT-III assemblies is regulated by Vps4 to mediate membrane remodelling during cytokinesis. Nature cell biology *19*, 787-798.
29. Batz, T., Forster, D., and Luschnig, S. (2014). The transmembrane protein Macroglobulin complement-related is essential for septate junction formation and epithelial barrier function in Drosophila. Development *141*, 899-908.
30. Furuse, M., and Tsukita, S. (2006). Claudins in occluding junctions of humans and flies. Trends in cell biology *16*, 181-188.
31. Lamb, R.S., Ward, R.E., Schweizer, L., and Fehon, R.G. (1998). Drosophila coracle, a member of the protein 4.1 superfamily, has essential structural functions in the septate junctions and developmental functions in embryonic and adult epithelial cells. Molecular biology of the cell *9*, 3505-3519.
32. Genova, J.L., and Fehon, R.G. (2003). Neuroglian, Gliotactin, and the Na+/K+ ATPase are essential for septate junction function in Drosophila. The Journal of cell biology *161*, 979-989.
33. Schwabe, T., Bainton, R.J., Fetter, R.D., Heberlein, U., and Gaul, U. (2005). GPCR signaling is required for blood-brain barrier formation in drosophila. Cell *123*, 133-144.
34. Paul, S.M., Ternet, M., Salvaterra, P.M., and Beitel, G.J. (2003). The Na+/K+ ATPase is required for septate junction function and epithelial tube-size control in the Drosophila tracheal system. Development *130*, 4963-4974.
35. Ikenouchi, J., Furuse, M., Furuse, K., Sasaki, H., Tsukita, S., and Tsukita, S. (2005). Tricellulin constitutes a novel barrier at tricellular contacts of epithelial cells. The Journal of cell biology *171*, 939-945.
36. Oda, Y., Otani, T., Ikenouchi, J., and Furuse, M. (2014). Tricellulin regulates junctional tension of epithelial cells at tricellular contacts through Cdc42. Journal of cell science *127*, 4201-4212.
37. Krug, S.M., Amasheh, S., Richter, J.F., Milatz, S., Gunzel, D., Westphal, J.K., Huber, O., Schulzke, J.D., and Fromm, M. (2009). Tricellulin forms a barrier to macromolecules in tricellular tight junctions without affecting ion permeability. Molecular biology of the cell *20*, 3713-3724.

38. Byri, S., Misra, T., Syed, Z.A., Batz, T., Shah, J., Boril, L., Glashauser, J., Aegerter-Wilmsen, T., Matzat, T., Moussian, B., et al. (2015). The Triple-Repeat Protein Anakonda Controls Epithelial Tricellular Junction Formation in Drosophila. Developmental cell *33*, 535-548.
39. Schulte, J., Tepass, U., and Auld, V.J. (2003). Gliotactin, a novel marker of tricellular junctions, is necessary for septate junction development in Drosophila. The Journal of cell biology *161*, 991-1000.
40. Hildebrandt, A., Pflanz, R., Behr, M., Tarp, T., Riedel, D., and Schuh, R. (2015). Bark beetle controls epithelial morphogenesis by septate junction maturation in Drosophila. Developmental biology *400*, 237-247.
41. Denk, W., and Horstmann, H. (2004). Serial block-face scanning electron microscopy to reconstruct three-dimensional tissue nanostructure. PLoS biology *2*, e329.
42. Steigemann, P., Wurzenberger, C., Schmitz, M.H., Held, M., Guizetti, J., Maar, S., and Gerlich, D.W. (2009). Aurora B-mediated abscission checkpoint protects against tetraploidization. Cell *136*, 473-484.
43. Sanger, J.M., Pochapin, M.B., and Sanger, J.W. (1985). Midbody sealing after cytokinesis in embryos of the sea urchin Arabacia punctulata. Cell Tissue Res *240*, 287-292.
44. Mierzwa, B., and Gerlich, D.W. (2014). Cytokinetic abscission: molecular mechanisms and temporal control. Developmental cell *31*, 525-538.
45. Lafaurie-Janvore, J., Maiuri, P., Wang, I., Pinot, M., Manneville, J.B., Betz, T., Balland, M., and Piel, M. (2013). ESCRT-III assembly and cytokinetic abscission are induced by tension release in the intercellular bridge. Science *339*, 1625-1629.
46. Ettinger, A.W., Wilsch-Brauninger, M., Marzesco, A.M., Bickle, M., Lohmann, A., Maliga, Z., Karbanova, J., Corbeil, D., Hyman, A.A., and Huttner, W.B. (2011). Proliferating versus differentiating stem and cancer cells exhibit distinct midbody-release behaviour. Nature communications *2*, 503.
47. Elia, N., Ott, C., and Lippincott-Schwartz, J. (2013). Incisive imaging and computation for cellular mysteries: lessons from abscission. Cell *155*, 1220-1231.
48. Chai, Y., Tian, D., Yang, Y., Feng, G., Cheng, Z., Li, W., and Ou, G. (2012). Apoptotic regulators promote cytokinetic midbody degradation in C. elegans. The Journal of cell biology *199*, 1047-1055.
49. Crowell, E.F., Gaffuri, A.L., Gayraud-Morel, B., Tajbakhsh, S., and Echard, A. (2014). Engulfment of the midbody remnant after cytokinesis in mammalian cells. Journal of cell science *127*, 3840-3851.
50. Huang, J., Zhou, W., Dong, W., Watson, A.M., and Hong, Y. (2009). Directed, efficient, and versatile modifications of the Drosophila genome by genomic engineering. Proceedings of the National Academy of Sciences of the United States of America 106, 8284-8289.
51. Claret, S., Jouette, J., Benoit, B., Legent, K., and Guichet, A. (2014). PI(4,5)P2 Produced by the PI4P5K SKTL Controls Apical Size by Tethering PAR-3 in Drosophila Epithelial Cells. Current biology : CB 24, 1071-1079.
52. Lowe, N., Rees, J.S., Roote, J., Ryder, E., Armean, I.M., Johnson, G., Drummond, E., Spriggs, H., Drummond, J., Magbanua, J.P., et al. (2014). Analysis of the expression patterns, subcellular localisations and interaction partners of Drosophila proteins using a pigP protein trap library. Development 141, 3994-4005.
53. Martin, A.C., Kaschube, M., and Wieschaus, E.F. (2009). Pulsed contractions of an actin-myosin network drive apical constriction. Nature 457, 495-499.

54. Mavrakis, M., Azou-Gros, Y., Tsai, F.C., Alvarado, J., Bertin, A., Iv, F., Kress, A., Brasselet, S., Koenderink, G.H., and Lecuit, T. (2014). Septins promote F-actin ring formation by crosslinking actin filaments into curved bundles. Nature cell biology 16, 322-334.

55. Mathieu, J., Cauvin, C., Moch, C., Radford, S.J., Sampaio, P., Perdigoto, C.N., Schweisguth, F., Bardin, A.J., Sunkel, C.E., McKim, K., et al. (2013). Aurora B and cyclin B have opposite effects on the timing of cytokinesis abscission in Drosophila germ cells and in vertebrate somatic cells. Developmental cell 26, 250-265.

56. Matusek, T., Wendler, F., Poles, S., Pizette, S., D'Angelo, G., Furthauer, M., and Therond, P.P. (2014). The ESCRT machinery regulates the secretion and long-range activity of Hedgehog. Nature 516, 99-103.

57. Calleja, M., Moreno, E., Pelaz, S., and Morata, G. (1996). Visualization of gene expression in living adult Drosophila. Science 274, 252-255.

58. Mlodzik, M., Baker, N.E., and Rubin, G.M. (1990). Isolation and expression of scabrous, a gene regulating neurogenesis in Drosophila. Genes & development 4, 1848-1861.

FIGURE LEGENDS

Figure 1: Midbody assembles and displaces toward the basal pole

(A-B) Time-lapse of dividing cells expressing MyoII::RFP (magenta) with E-Cad::GFP (A, cyan, n>30; see also Movie S1) or ATPα::YFP (B, green, n>30). Cyan line highlights the level of AJ and red arrows point to the midbody.

(C) Plot of the quantitation of the apical to basal movement of the midbody over time relative to AJ (cyan line: 0 to -0.5 µm) and SJ (green line: -0.5 to -3 µm) (n=20).

(D) Kymographs and quantitation of the residence time of MyoII::RFP (n=66), Sep2::GFP (n=45), Pnut::mCherry (n=18), LifeAct::mCherry (n=27) or Jupiter::GFP (n=20; see also Movie S2) present in the midbody.

(E) Kymographs of MyoII::RFP (magenta) imaged with Sep2::GFP (green) present in the midbody over time in control condition (left panels) or upon photobleaching (right panels). Photobleaching of MyoII::RFP was done 10 minutes following contractile ring constriction (yellow dashed line); see also Movies S3 and S4.

(F) Plot of the quantitation of the fluorescence signal recovery of MyoII::RFP (n=7) after photobleaching over time.

(G-J) TEM micrographs of dividing notum cells sectioned along the apico-basal axis and parallel to the midbody. H is a high magnification of the inset depicted in G. Three stages of midbody are shown: maturing midbody (H, n>20; see also Movie S5), intermediate midbody (I, n>20; see also Movie S6) and intercellular bridge (J, n>20; see also Movie S7).

(K-M) Top view (K) or orthogonal sections (L-M) showing the distribution of maturating midbody (magenta), intermediate midbody (green) and intercellular bridges (cyan) identified using the SFB-SEM volume reconstitution. M is a maximal projection of orthogonal sections depicted in L. Two daughter cells (cyan and blue) and their two neighbors (yellow and orange) were represented; see also Movie S8.

Time is in hour:minute (A-B) or in minutes (C-F), with t=0 min corresponding to the onset of anaphase. Scale bars represent 3 µm (A-B) or 200 nm (H-J). Ap: apical; B: basal. **See also Figure S1 and Figure S2.**

Figure 2: Abscission is temporally uncoupled to Shrb recruitment.

(A) Serial TEM sections of WID cells parallel to the intercellular bridge (n>20). Abscission occured at one extremity of the bridge (red arrow) while the other extremity remained open on the cytoplasm (yellow arrow). Numbers refer to the distance (nm) that separates the sections.

(B) TEM micrographs of WID epithelial cells sectioned parallel to the degrading intercellular bridge (n>20). The cytoplasm is colored in cyan.

(C) Kymographs and quantitation of the residence time of AurB::GFP (n=7), Svv::GFP (n=7) or Shrb::GFP (n=10) present in the midbody.

(D) Time-lapse of dividing cells expressing ATPα::YFP (green) and KAEDE. Green to red (magenta) photoconversion of KAEDE was done (yellow lightning) in one daughter cell 3 hours following the onset of anaphase of the mother cell and cytoplasmic equilibration was observed (n=16 from 1h45 to 5h). Yellow line delineates the dividing cell and its daughters.

Time is in hour:minute (D) or in minutes (C), with t=0 min corresponding to anaphase onset (C) or the time of photoconversion (D). Scale bars represent 3 µm (D) or 200 nm (A-B). **See also Figure S3.**

Figure 3: Dividing cells remain connected to their neighbors throughout cytokinesis.

(A) Time-lapse of a dividing cell expressing MyoII::RFP (magenta) with ATPα::YFP (green) (n>30). Orange line highlights the contact of the neighbors and the dividing cell.

(B-C) Time-lapse of a clone of cells expressing MyoII::RFP (magenta) and surrounded by cells expressing MyoII::RFP with ATPα::YFP (green, with nls-GFP) (n=18). Yellow line highlights a dividing cell devoid of ATPα::YFP, identified by the loss of nls-GFP. (C) is a high magnification of the red inset depicted in (B).

(D-H) 3D model based on SFB-SEM dataset illustrating the membrane contact made between daughter cells (cyan and blue) and their neighbors (yellow and orange). At AJ level, the daughters have assembled a long adhesive interface (E); while at SJ level, they are connected by the midbody (green) (F). Orthogonal views of daughters (G) and of neighbors with the finger-like protrusions (H), both connected to the midbody (green).

(I-K) TEM micrograph of dividing notum epithelial cells sectioned parallel to the midbody (I) and ultrathin serial sections parallel (J) or orthogonal (K) to the midbody. Neighbor cells (yellow and orange) are tightly connected to the dividing cells.

Time is in hour:minute (A-C), with t=0 min corresponding to anaphase onset. Cyan line highlights the position of AJ and red arrows point to the midbody. Distances correspond to the position relative to the plane of AJ labeled with MyoII::RFP. Scale bars represent 3 µm (A-C), 2 µm (I) or 200 nm (J-K). **See also Figure S4.**

Figure 4: *De novo* assembly of SJ at the cleavage site.

(A) Time-lapse of a dividing clonal cell expressing MyoII::RFP (magenta) with ATPα::YFP (green) (identified by the loss of nls-RFP, not shown) and surrounded by cells devoid of ATPα::YFP (n=13).

(B) Time-lapse of a dividing cell expressing MyoII::RFP (magenta) with Gli::YFP (green) (n=11). High magnifications on right panels correspond to the red inset depicted at t=10 min. Yellow arrows show the first Gli::YFP puncta and white arrow shows the final Gli::YFP distribution at TSJ.

Time is in hour:minute, with t=0 min corresponding to anaphase onset. Yellow line delineates the dividing cell and its daughters, cyan lines highlight the position of AJ and red arrows point to the midbody. Distances correspond to the position relative to the plane of AJ labeled with MyoII::RFP. Scale bars represent 3 µm. **See also Figure S5.**

Figure 5: New SJ junctions assemble apically.

(A-C) Time-lapse of dividing (A) or interphase (B-C) cells expressing MyoII::RFP (magenta) with ATPα::YFP (A-B, green) or Bark::GFP (C, green). The photobleached ROI correspond to the yellow insets.

(D-F) Kymographs representing the photobleaching of ATPα::YFP (D-E, green) or Bark::GFP (F, green) imaged with MyoII::RFP (magenta). Yellow lines indicate the time of photobleaching.

(G-I) Plots of the quantitation of fluorescence recovery of ATPα::YFP (G-H) or Bark::GFP (I) after photobleaching over time. Black, blue and red curves correspond to 1 µm, 2 µm below AJ level and midbody level, respectively (G, n=10; H, n=16; I, n=12).

Time is in hour:minute (A-C) or in minutes (D-I), with t=0 min corresponding to the time of photobleaching. Distances correspond to the position relative to the plane of AJ labeled with MyoII::RFP. Scale bars represent 3 µm.

Figure 6: SJ components regulate midbody basal displacement.

(A-B, F-G) Time-lapse of wild-type (A, F), *nrv2*^{k13315} mutant (B) or *bark*^{L200} mutant (G) dividing cells expressing MyoII::RFP (magenta, with nls-RFP) with ATPα::YFP (green).

(C, H) Plots of the quantitation of fluorescence recovery of ATPα::YFP after photobleaching over time in wild-type (black, C, n=10; H, n=16), *nrv2*^{k13315} mutant (red, C, n=10) or *bark*^{L200} mutant (blue, H, n=7) cells 1 µm below AJ.

(D, I) Time-lapse of *nrv2*^{k13315} mutant (D) or *bark*^{L200} mutant (I) dividing cells expressing MyoII::RFP (magenta, with nls-RFP) with ATPα::YFP (D, green) or E-Cad::GFP (I, cyan); see also Movie S9.

(E, J) Plots of the quantitation of the apical to basal movement of the midbody over time relative to AJ (cyan line: 0 to -0.5 µm) for wild-type (black, n=20), *nrv2*^{k13315} mutant (C, red, n=20) or *bark*^{L200} mutant (F, blue, n=20) cells.

Time is in hour:minute (A-B, D, F-G, I) or in minutes (C, E, H, J), with t=0 min corresponding to anaphase onset (A-B, D-G, I-J) or the time of photobleaching (C, H). Yellow lines delineate the clone border and mutant cells are identified by the loss of nls-RFP (yellow stars), cyan lines highlight the level of AJ and white arrows point to the midbody. Scale bars represent 3 µm. **See also Figure S6.**

Figure 7: Model of SJ remodeling during cytokinesis.

After contractile ring closure, a long adhesive interface is assembled between daughter cells (cyan and blue) at AJ level. At SJ level, neighboring cells (yellow and orange) exhibit membrane protrusions that maintain cell-cell contacts with the dividing cell at the level of the midbody (magenta), forming a *ménage à quatre*. TSJ (light green), first detected in dotted structures just above the midbody, evolve as a line as the midbody descents basally and are ultimately found at the tricellular contacts contacts between the daughter and the neighbors. Concomitantly, BSJ (dark green) assembles below AJ and above the midbody and this apical to basal outspreading of BSJ thus drives the basal displacement of the midbody and membrane protrusions. Upon completion of SJ assembly, the midbody leaves the SJ belt and moves faster towards the basal pole.

STAR METHODS

CONTACT FOR REAGENT AND RESOURCE SHARING

Further information and requests for resources and reagents should be directed to and will be fulfilled by the Lead Contact, Roland Le Borgne (roland.leborgne@univ-rennes1.fr).

EXPERIMENTAL MODEL AND SUBJECT DETAILS

Drosophila stocks and genetics

Drosophila melanogaster stocks were maintained and crossed at 25°C.

Somatic clones were induced using the FLP-FRT technique using the *hs*-FLP and by two heat shocks (60 min at 37°C) at second and third instar larvae.

The *ap*-GAL4 or *pnr*-GAL4 drivers were used to drive the expression of UAS-Pnut::mCherry, UAS-LifeAct::RFP or UAS-AurB::GFP. The expression of UAS-Shrb::GFP was driven by the *ay*-GAL4 driver. Finally, the *sca*-GAL4 driver was used to drive the expression of the photoconvertible probe UAS-KAEDE.

MyoII::RFP (also called Sqh above) flies were designed and generated by *inDroso functional genomics* (Rennes, France) using CRISPR-mediated HR. RFP was inserted just before the stop codon of endogenous *MyoII* gene with a flexible GVG linker and the resulting flies was validated by sequencing.

Drosophila genotypes

All EM experiments have been performed on w^{118} strain (Figures 1G-M, 2A-B, 3D-K).

Figure 1

- (A) y, w, sqh^{AX3}; DE-Cad::GFP^{GE23}/*sqh*-Sqh::RFP
- (B) y, w, sqh^{AX3}; *sqh*-Sqh::RFP/+; ATPα::YFP/+
- (C) sqh::RFP^{crispr}
- (D) y, w, sqh^{AX3}; *sqh*-Sqh::RFP – *ap*-GAL4, Sep2::GFP/+; *UAS-mCherry::Pnut/*+ – *ap*-GAL4, Sep2::GFP/*UAS-LifeAct::RFP* – y, w, sqh^{AX3}; *sqh*-Sqh::RFP/+; Jupiter::YFP/+
- (E-F) y, w, sqh^{AX3}; *ap*-GAL4, Sep2::GFP/*sqh*-Sqh::RFP

Figure 2

- (C) *pnr*-GAL4/UAS-AurB::GFP – y, w, *sqh*^{AX3};; *sqh*-Sqh::mCherry/Svv::GFP – hs-FLP/y, w, *sqh*^{AX3} ; *Ay*-GAL4/UAS-Shrb ::GFP ; *sqh*-Sqh ::mCherry/+
- (D) *sca*-GAL4/+; ATPα::YFP/UAS-KAEDE

Figure 3

- (A) y, w, *sqh*^{AX3}; *sqh*-Sqh::RFP/+; ATPα::YFP/+
- (B-C) y, w, *hs*-FLP/y, w, *sqh*^{AX3}; *sqh*-Sqh::RFP/+; FRT82B, Ubi-GFP nls/FRT82B, ATPα::YFP

Figure 4

- (A) y, w, *hs*-FLP/y, w, *sqh*^{AX3}; *sqh*-Sqh::RFP/+; FRT82B, Ubi-RFP nls/FRT82B, ATPα::YFP
- (B) y, w, *sqh*^{AX3}; *sqh*-Sqh::RFP/Gli::YFP

Figure 5

- (A-B, D-E, G-H) sqh::RFP^{crispr};; ATPα::YFP/+
- (C, F, I) sqh::RFP^{crispr}; Bark::GFP/+

Figure 6

- (A-E) y, w, *hs*-FLP/y, w, *sqh*^{AX3}; Ubi-RFP nls, FRT40A/*nrv2*^{k13315}, FRT40A; ATPα::YFP, *sqh*-Sqh::mCherry/+
- (F-I) y, w, *hs*-FLP/y, w, *sqh*^{AX3}; Ubi-RFP nls, FRT40A/*bark*^{L200}, FRT40A; ATPα::YFP, *sqh*-Sqh::mCherry/+
- (J) sqh::RFP^{crispr}/y, w, *hs*-FLP; Ubi-RFP nls, FRT40A, DE-Cad::GFP^{GE23}/*bark*^{L200}, FRT40A

METHOD DETAILS

Immunofluorescence

Pupae aged for 16h30 to 18h after puparium formation (APF) were dissected using Cannas microscissors in 1X Phosphate-Buffered Saline (1X PBS, pH 7.4) and fixed 15 min in 4% paraformaldehyde at room temperature [18]. Following fixation, dissected nota were permabilized using 0.1% Triton X-100 in 1X PBS (PBT), incubated with primary antibodies diluted in PBT for 2 hours at room temperature. After 3 washes of 5 minutes in PBT, nota were

incubated with secondary antibodies diluted in PBT, followed by 2 washes in PBT, and one wash in PBS, prior mounting in 0,5% N-propylgallate dissolved in 1X PBS + 90% glycerol.

Live-imaging and image analyses

Live imaging was performed on pupae aged for 16h30 APF at 20-25°C [18]. Pupae were sticked on a glass slide with a double-sided tape, and the brown pupal case was removed over the head and dorsal thorax using microdissecting forceps. Pillars made of 4 to 5 glass coverslips were positioned at the anterior and posterior side of the pupae, respectively. A glass coverslip covered with a thin film of Voltalef 10S oil is then placed on top of the pillars such that a meniscus is formed between the dorsal thorax of the pupae and the glass coverslip. Images were acquired with a LSM Leica SP5 or SP8 equipped with a 63X N.A. 1.4. and controlled by LAS AF software. Confocal sections were taken every 0.5 µm. All images were processed and assembled using ImageJ/FIJI software and Adobe Illustrator.

Midbody tracking

The 3D coordinates of the midbody were manually tracked over time to be artificially realigned to generate the kymographs.

The apico-basal position of the midbody was calculated measuring the distance between the middle of the new AJ and the midbody (both labelled with MyoII::RFP) at each time. The x, y, z coordinates of AJ and midbody were manually tracked to record positions at each time, and then are used to calculate the distance using the Pythagorean Theorem.

KAEDE photoconversion

Photoconversion assays were performed in pupae expressing the green to red photoconvertible probe KAEDE. KAEDE was photoconverted (405 nm laser at 0.1% power, point bleach, 4 iterations of 100 ms each) using a LSM Leica SP8 equipped with a 63X N.A. 1.4 PlanApo objective. Confocal stacks were acquired every 5 min after photoconversion.

Fluorescence recovery after photobleaching

FRAP experiments were performed in pupae expressing MyoII::RFP or Pnut::mCherry together with Sep2::GFP used as a marker of midbody. MyoII::RFP and Pnut::mCherry were bleached (561 nm laser at 40% or 30% power, respectively, point bleach, one iteration of 500 ms) using a LSM Leica SP5 and a 63X N.A. 1.4 PlanApo objective. Confocal stacks were acquired every 2 min after photobleaching.

FRAP experiments were performed in pupae expressing ATPα::YFP or Bark::GFP together with MyoII::RFP. Regions of interest corresponding to the entire junctions (interphase cells) or the finger-like protrusions pointing to the midbody (mitotic cells) were bleached (488 nm laser at 100% power, 1 iteration of 100 ms) using a LSM Leica SP5 or SP8 equipped with a 63X N.A. 1.4 PlanApo objective. Confocal stacks were acquired every 5 min after photobleaching.

TEM sample preparation

Drosophila wing discs (third instar larvae) and pupal notum (16h APF) were dissected in PBS at room temperature and immediately processed [83, 84]. Briefly, the samples were fixed in 1% paraformaldehyde and 2.5% glutaraldehyde in 0.1M cacodylate buffer for 2 hours. Then, they were stained for 1 hour in 2% (wt/vol) osmium tetroxide and 1.5% (wt/vol) $K_4[Fe(CN)_6]$ in cacodylate buffer followed by 1 hour in 1% (wt/vol) tannic acid in 100 mM cacodylate buffer. Finally, they were incubated 30 min in 2% (wt/vol) osmium tetroxide followed by 1% (wt/vol) uranyl acetate for 2 hours. After the dehydration cycles, samples were embedded in Epon-Araldite mix. To assure precise orientation and access to the samples 2-step flat embedding procedure was used [84].

TEM observation and analysis

Rigid flat blocks were trimmed using 90° diamond trim tool (Diatome, Biel, Switzerland) to delimit the zone of interest based on laser marks. For standard TEM observations, samples were directly processed to thin sectioning using 35° diamond knife (Diatome, Biel, Switzerland). For high-resolution analyses, sections were collected on formvar-coated slot grids (EMS) and analyzed with a JEOL JEM-1400 electron microscope operated at 80kV, equipped with a Gatan Orius SC 1000 camera, piloted by the Digital Micrograph program.

For 3-view analysis, flat blocks were glued onto an aluminum cryo specimen pin using superglue (cyanoacrylate, Permabond). For trimming, care was taken to orient the sample so that the imaging plane was perpendicular to the pin axis to form a trapezoid face approximately 500 x 500 x 150 µm before mounting on a Gatan 3-view within an FEI Quanta 250 FEG scanning electron microscope. For the purpose of this study the imaging settings were: accelerating voltage: 3.8kV; spot size: 3.5; final lens aperture: 30 µm; chamber pressure: 66 Pa; quadrant magnification: 3500x giving a horizontal field width of approximation 40 µm; image dimensions: 4096 x 4096; pixel dwell time: 10 µs; cut thickness: 100nm.

Raw data was converted to an MRC file stack using IMOD [83]. Imaging noise was removed by a standard Gaussian smoothing using a 3x3 kernel in order to aid manual segmentation. TEM

data analysis was performed using FIJI, IMOD 3Dmod module for particular regions annotations and modelling. Photoshop was used for alignment of serial sections and pseudo-coloring of different zones in image.

QUANTIFICATION AND STATISTICAL ANALYSIS

Signal recovery upon photobleaching

On kymographs focused on junctions at -1 µm, -2 µm or at midbody level (level 0 corresponds to the AJ level), the mean of fluorescence intensity was measured on 13 pixels along the time.

In FRAP experiments on MyoII::RFP or Pnut::mCherry, this was performed for the photobleached midbody, control midbody (another non-FRAP cell at the same stage of division) and 3 backgrounds. In FRAP experiments on ATPα::YFP or Bark::GFP, this was performed for the photobleached junctions, control junctions (3 for interphase cell assay, 1 for mitotic cell assay) and 3 backgrounds. Note that in mitotic cells, the control junction is the finger-like protrusion opposite to the FRAPed finger-like protrusion.

The differences between averaged controls and averaged backgrounds were normalized with 3 pre-FRAP values to 1 and approximated by an order 2 polynomial model (trend). Finally, the photobleached midbody/junction values are subtracted from the averaged backgrounds, normalized with 3 pre-FRAP values to 1 and divided by the trend over time to give the fluorescence ratio.

For FRAP experiments on ATPα::YFP in wild-type and *bark*^{L200} mutant cells and on Bark::GFP, fluorescence ratios were approximated with a linear model of type: $y = ax + b$, where a and b are 2 constants. For FRAP experiments on ATPα::YFP in *nrv2*^{k13315} mosaic tissue, fluorescence ratios were approximated with an exponential model of type: $y = a\,e^{-x/\tau} + Y_0$, where a, τ and Y_0 are 3 constants. The Y_0 parameter has been added to the usual exponential model, because data do not start to 0. Finally, halftimes were calculated with the equation: $t_{1/2} = -\ln(0.5) / \tau$.

Statistical tests

All information concerning the statistical details are provided in the main text and in figure legends, including the number of samples analyzed for each experiment. Histograms use the following standards: boxes limits indicate the means and errors bars represent the standard deviations. Boxplots use the following standards: centerlines of boxes show the medians; boxes limits indicate the 25th and 75th percentiles; whiskers extend 1.5 times the interquartile range

from the 25th and 75th percentiles. For the representation of the data in the main Figure 6C: all values are represented by dots; the thick line indicate the average and the errors bars represent the standard deviations.

Statistical analyses were performed using the R software version 1.0.136. First, for the analysis of midbody displacement curves from t=0 to t=110 min following the anaphase onset, we performed an ANCOVA to compare the effect of the interaction between time and the “condition” parameter (wild-type versus mutant). Second, for the analysis of FRAP experiments in wild-type and *bark*^{L200} mosaic tissue, we performed an ANOVA to test the effect of the “condition” parameter (interphase versus mitotic, wild-type versus mutant). Residues follow a normal distribution (Shapiro test) and data are controlled for random effects (individual variability). For FRAP experiments on *nrv2*^{k13315} mosaic tissue, t-tests (data follow a normal distribution – Shapiro test) were applied to compared halftimes and percentages of recovery between wild-type and mutant cells.

Statistical significances were represented as follow: p-value > 0.05 NS (not significant); p-value ≤ 0.05 *; p-value ≤ 0.01 *** and p-value ≤ 0.001 ***.

MOVIE LEGENDS

Movie S1: Time-lapse of a dividing cell expressing MyoII::RFP (magenta) with E-Cad::GFP (blue), related to Figure 1A

Movie S2: Time-lapse of a dividing cell expressing MyoII::RFP (magenta) with Jupiter::GFP (green), related to Figure 1D

Movie S3: Time-Lapse of a dividing cell expressing Sep2::GFP (green) and MyoII-RFP (magenta), related to Figure 1E.
Control cell for FRAP experiment. Top view, single confocal section at the level of the midbody

Movie S4: Time-Lapse of FRAP of a dividing cell expressing Sep2 (green) and MyoII-RFP (magenta), related to Figure 1E.
FRAP of MyoII-RFP signal was performed at t= 10 min post anaphase onset. Top view, single confocal section at the level of the midbody,

Movie S5: Serial ultrathin sections of a dividing cell crossing a midbody containing interdigitated microtubules, related to Figure 1H.

Movie S6: Serial ultrathin sections of a dividing cell crossing a maturing midbody, **related to Figure 1I**.

Movie S7: Serial ultrathin sections of a dividing cell crossing an intercellular bridge, related to Figure 1J

Movie S8: SFB-SEM data set and 3D representation of the contacts made between daughter cells (blue and yellow) and their neighbors (cyan and magenta), related to Figure 1K-M.
Orthogonal sections corresponding to a total volume of 80x20x24 μm3 (240 sections).

Movie S9: Time-lapse of dividing *nrv2* mutant cells expressing MyoII::RFP (magenta) with ATP::YFP (green), related to Figure 6D
Left and right panels correspond to top views and orthogonal sections, respectively.

STAR METHODS

KEY RESOURCES TABLE

REAGENT or RESOURCE	SOURCE	IDENTIFIER
Antibodies		
Mouse anti-Coracle (1:200)	DSHB	C615.16
Mouse anti-Fasciclin 3 (1:200)	DSHB	7G10
Mouse anti-Gliotactin (1:100)	[39]	1F6.3
Cy2-, Cy3- and Cy5-coupled secondary antibodies (1:250)	The Jackson Laboratory	N./A.
Chemicals, Peptides, and Recombinant Proteins		
Cacodylate	Sigma	C4945
Cyanoacrylate	Manutan	A 008749
Epon Araldyte	Sigma	45345
Glutaraldehyde	EMS	19344-10
Osmium tetroxide	EMS	19152
Paraformaldehyde	EMS	19340-72
Phosphate Buffered Saline	Lonza	BE17-515F
Potassium ferricyanide	EMS	26604-1A
Tannic Acid	Sigma-Aldrich	403040
Triton X-100	Euromedex	2000 B
Uranyl acetate	Laurylab	48/851/13
Voltalef	VWR	24627.188
Experimental Models: Organisms/Strains		
D. melanogaster: w^{1118}	BDSC	BL3605
D. melanogaster: DE-Cad::GFP^{GE23}	[50]	N./A.
D. melanogaster: *tub*-RFP::PH_{GRP1}	[51]	N./A.

D. melanogaster: w;; ATPα::YFP/TM6C, *Tb*	[52], DGRC	115323
D. melanogaster: y, w, sqh^{AX3}; *sqh*-Sqh::RFP	R. Karess	N./A.
D. melanogaster: y, w, sqh^{AX3};; *sqh*-Sqh::mCherry	[53]	N./A.
D. melanogaster: sqh::RFP^{crispr}	This study	N./A.
D. melanogaster: y, w;; Sep2::GFP	BDSC	BL26257
D. melanogaster: UAS-mCherry::Pnut	[54]	N./A.
D. melanogaster: UAS-LifeAct::mCherry	F. Payre	N./A.
D. melanogaster: w;; Jupiter::YFP	DGRC	110606
D. melanogaster: UAS-AurB::GFP	[55]	N./A.
D. melanogaster: Svv::GFP	[55]	N./A.
D. melanogaster: *hs*-FLP; UAS-Shrb::GFP	[56]	N./A.
D. melanogaster: w;; UAS-KAEDE	BDSC	BL26161
D. melanogaster: y, w, *hs*-FLP;; FRT82B, Ubi-GFP nls	[51]	N./A.
D. melanogaster: FRT82B, ATPα::YFP/TM6C, *Tb*	[51]	N./A.
D. melanogaster: Gli::YFP	[52]	N./A.
D. melanogaster: Bark::GFP	[43]	N./A.
D. melanogaster: y, w, *hs*-FLP; Ubi-RFP nls, FRT40A	[60]	N./A.

D. melanogaster: *nrv2*^{k13315}, FRT40A/CyO	DGRC	114351
D. melanogaster: *bark*^{L200}, FRT40A/CyO	[38]	N./A.
D. melanogaster: *ap*-GAL4/CyO	[57]	N./A.
D. melanogaster: *pnr*-GAL4/TM6, *Tb*	[57]	N./A.
D. melanogaster: *sca*-GAL4/CyO	[58]	N./A.
D. melanogaster: *ay*-GAL4/CyO	BDSC	BL3953
Software and Algorithms		
Image J/FIJI	open source Java image processing program	https://imagej.nih.gov/ij/
R-Studio version 1.0.136	Open Source	https://www.rstudio.com/products/rstudio/download/
Illustrator	Adobe Systems	Adobe Illustrator CS6
Others		
confocal microscopy	Leica	LSM TCS SP5 and TCS SP8
Transmission Electron Microscope	JEOL	JEM-1400
Scanning Electron Microscope	FEI	Quanta 250 FEG

Figure 1

Click here to download Figure Figure1.tif

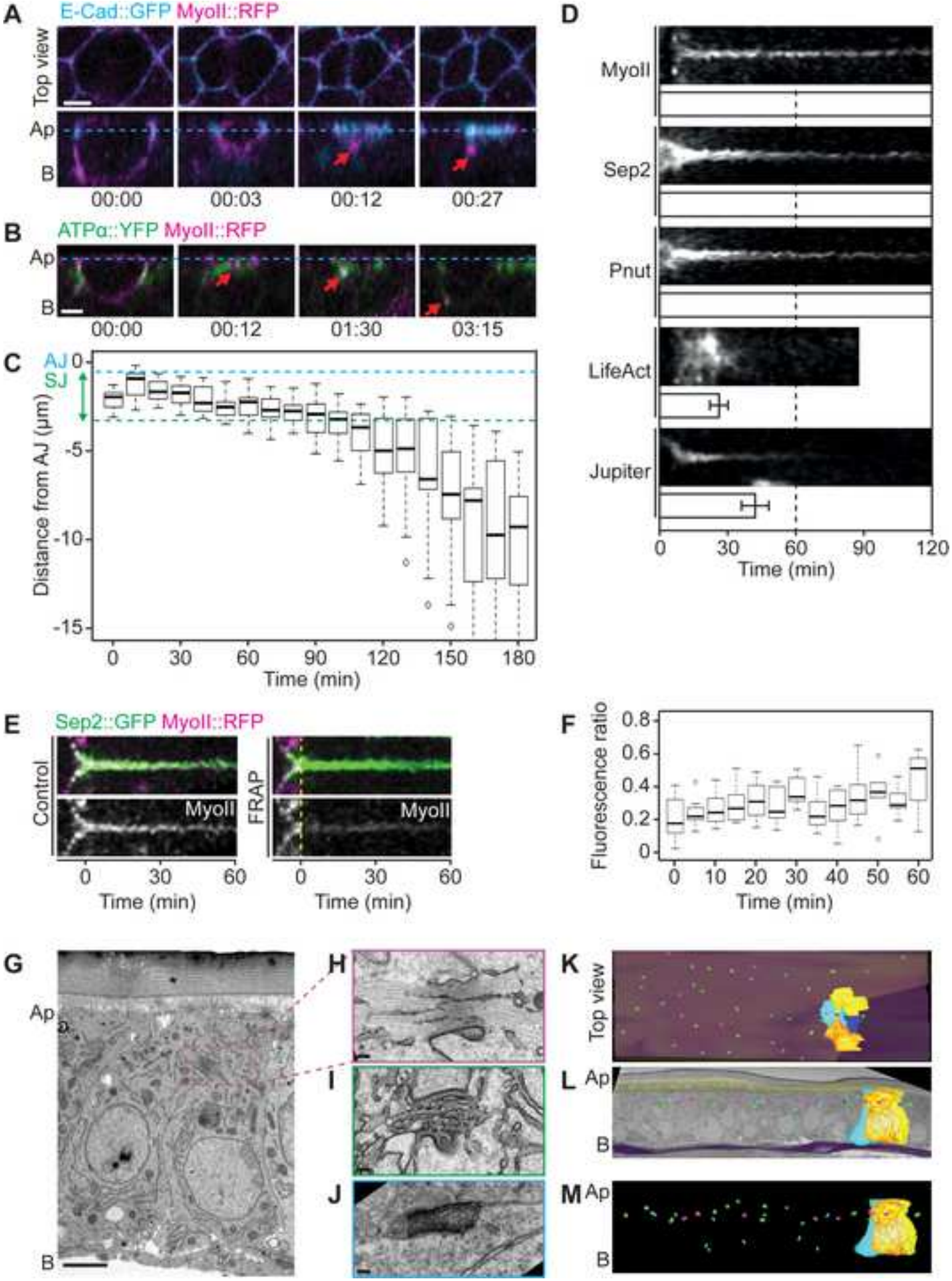

Figure 2

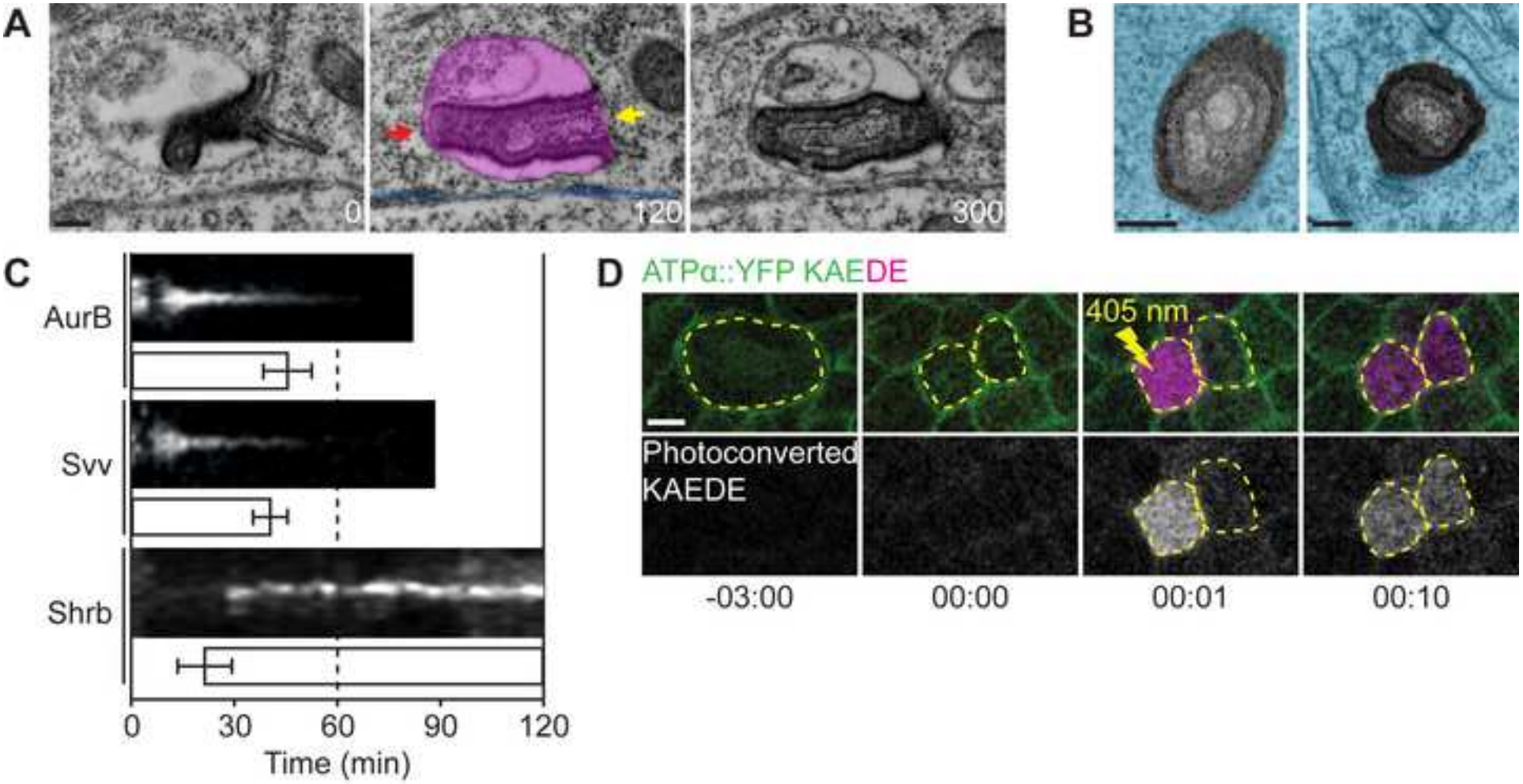

Figure 3

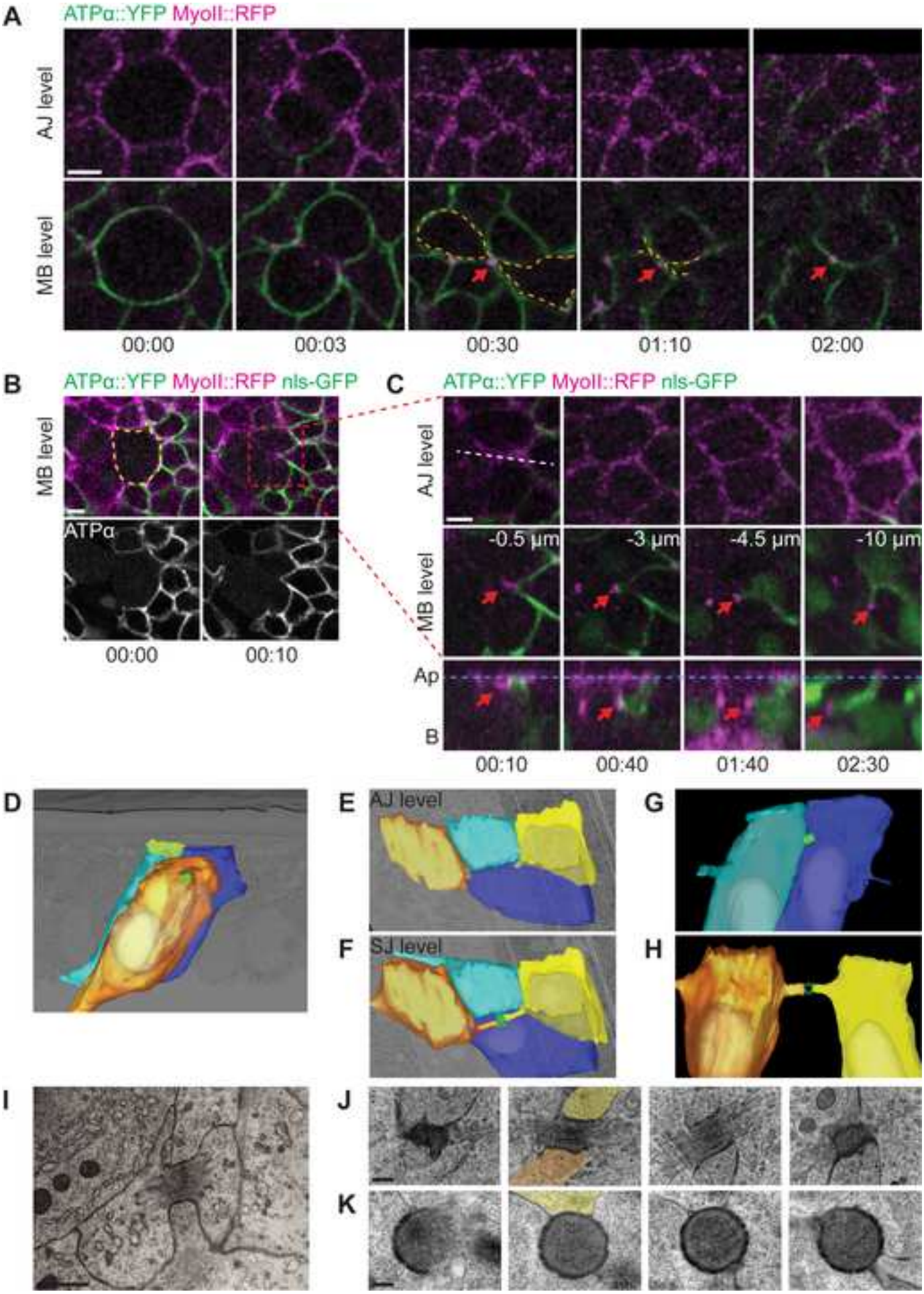

Figure 4

Click here to download Figure Figure4.tif

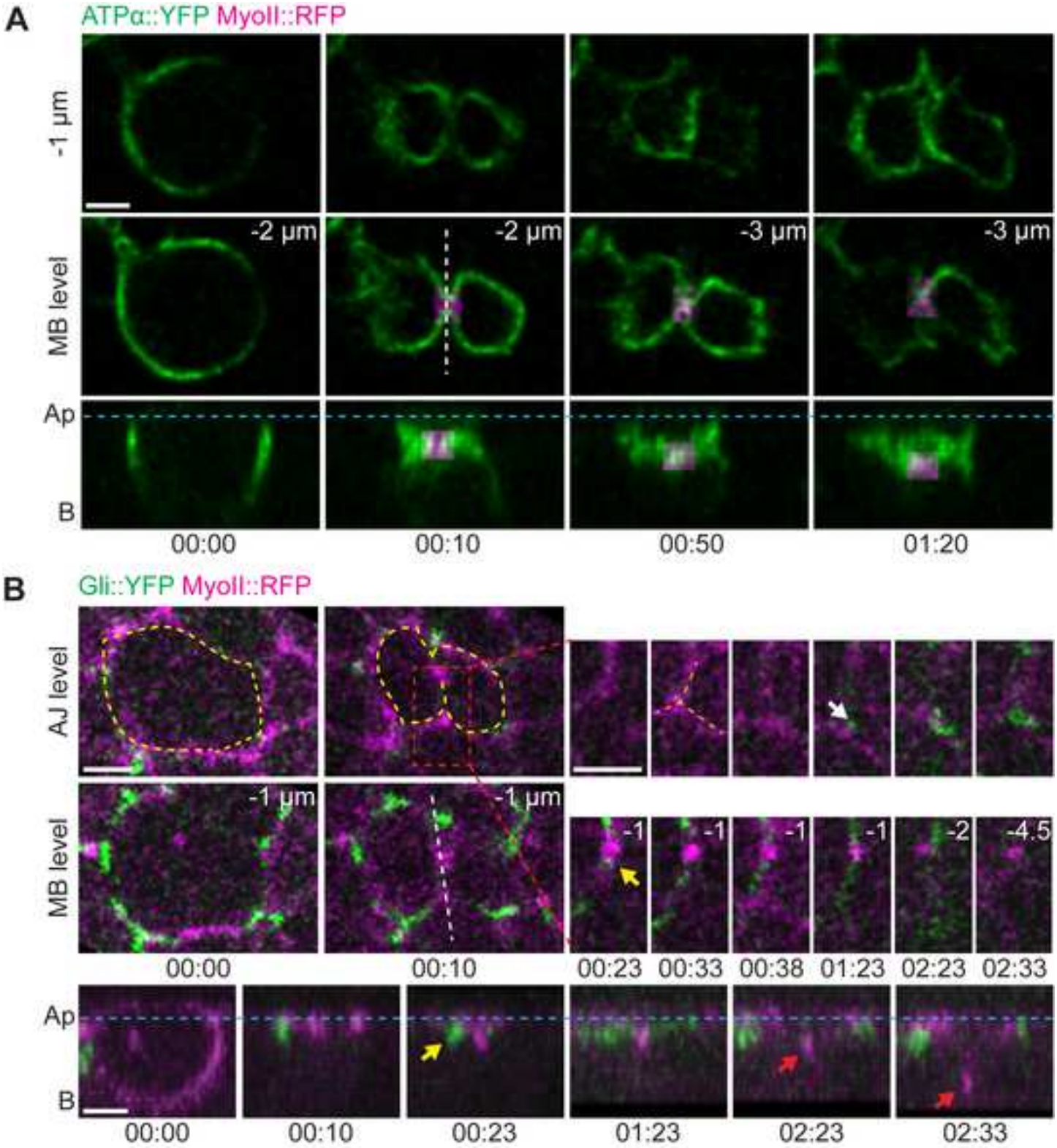

Figure 5

Click here to download Figure Figure5.tif

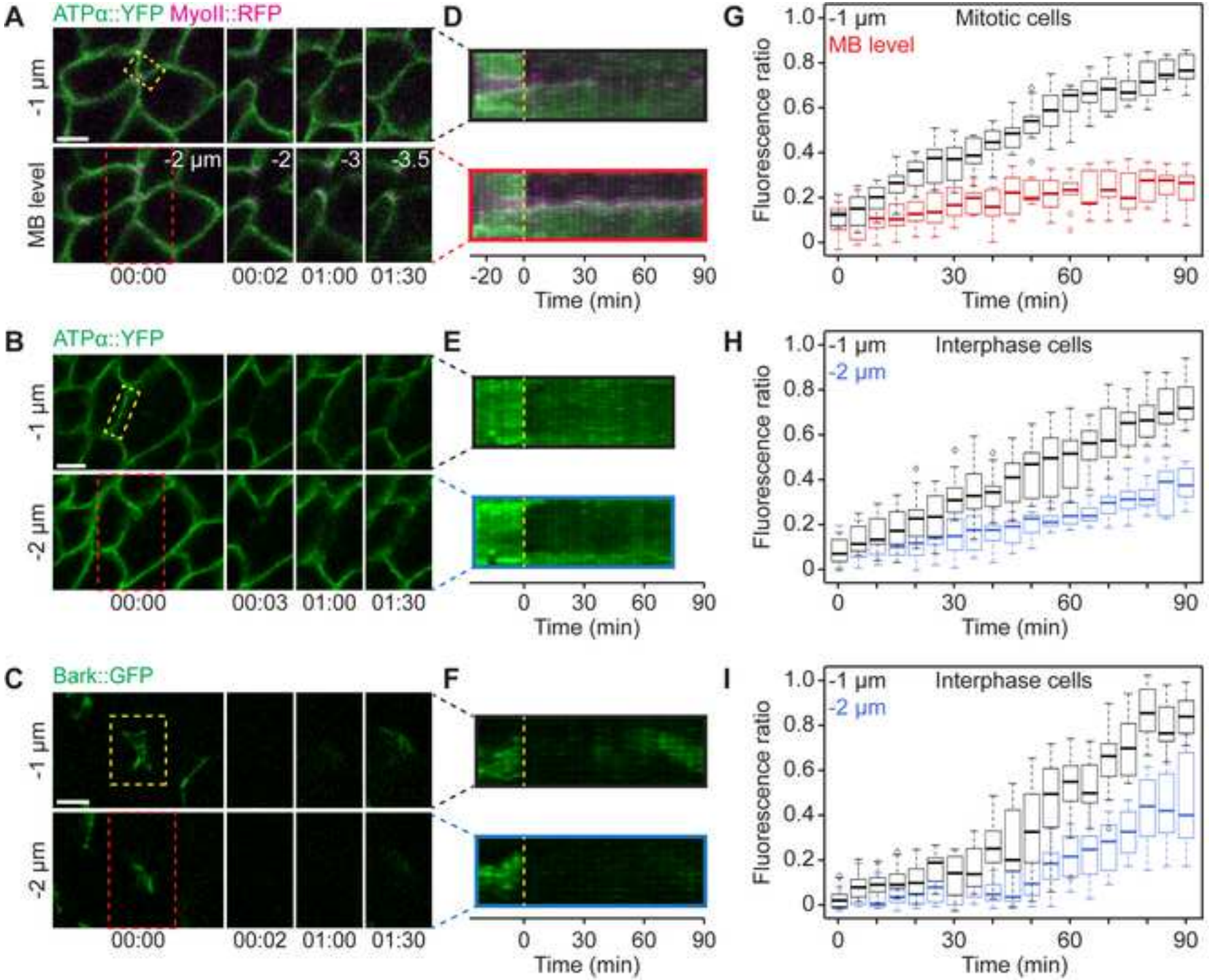

Figure 6

Click here to download Figure Figure6.tif

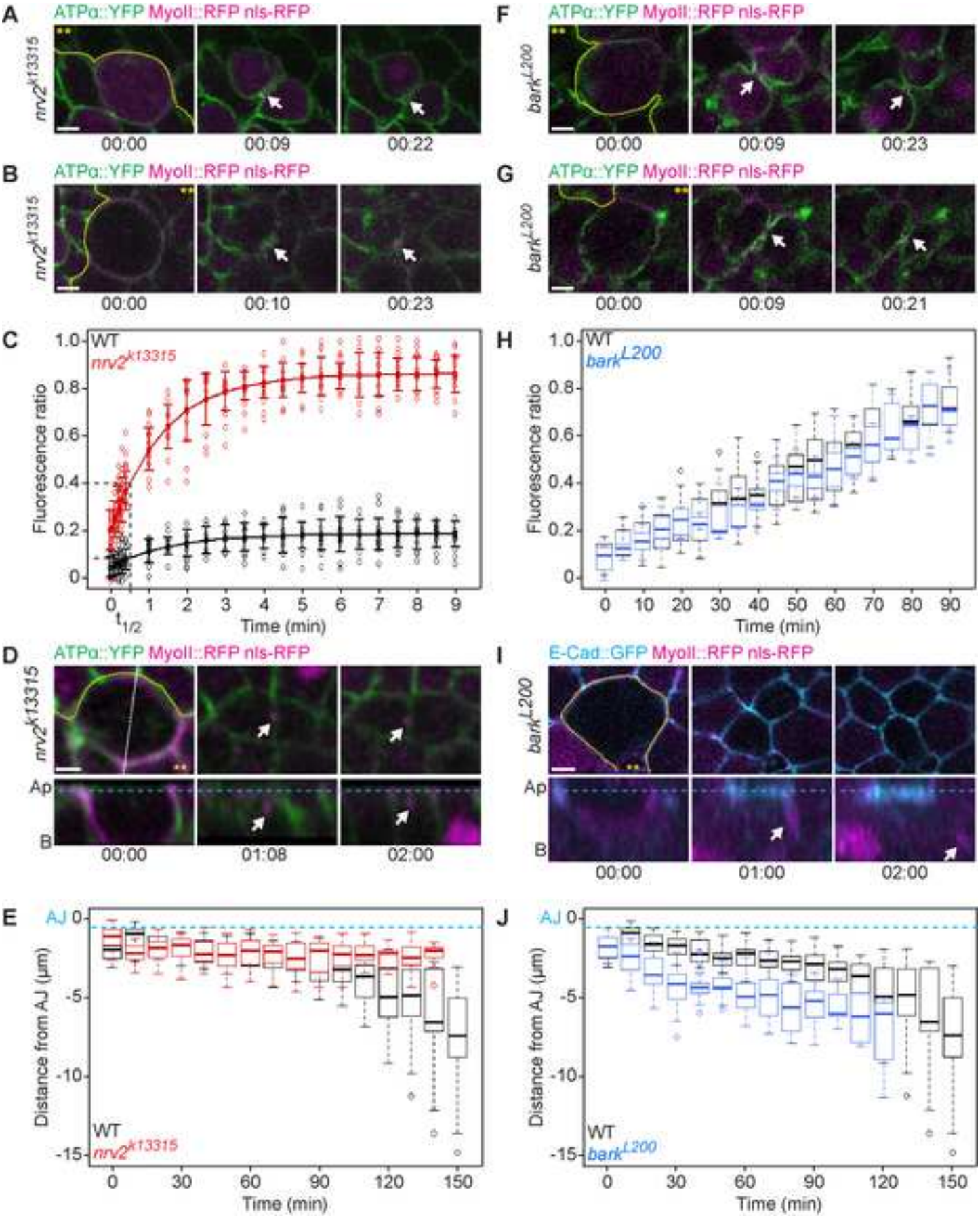

Figure 7

Click here to download Figure Figure7.tif

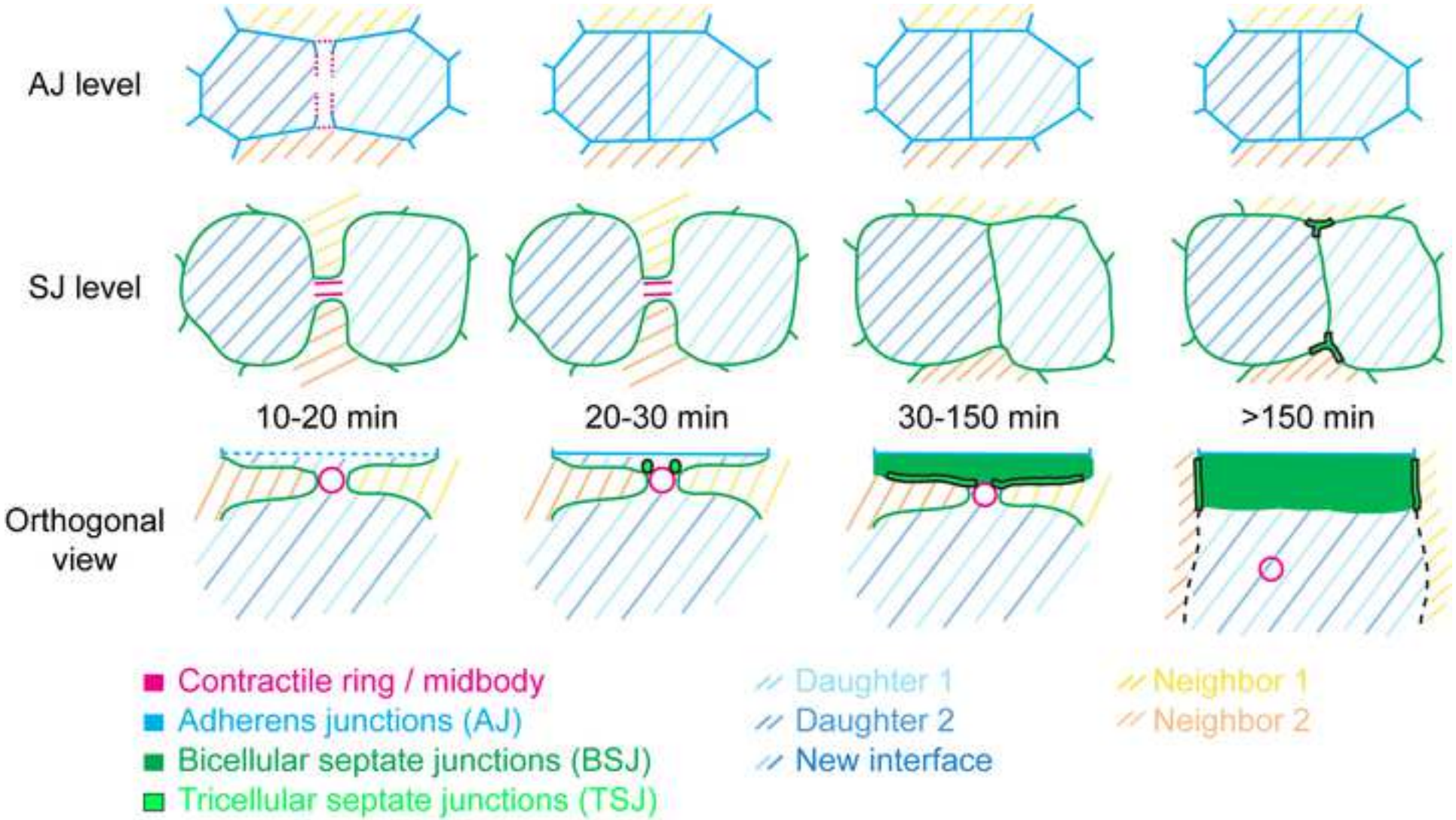

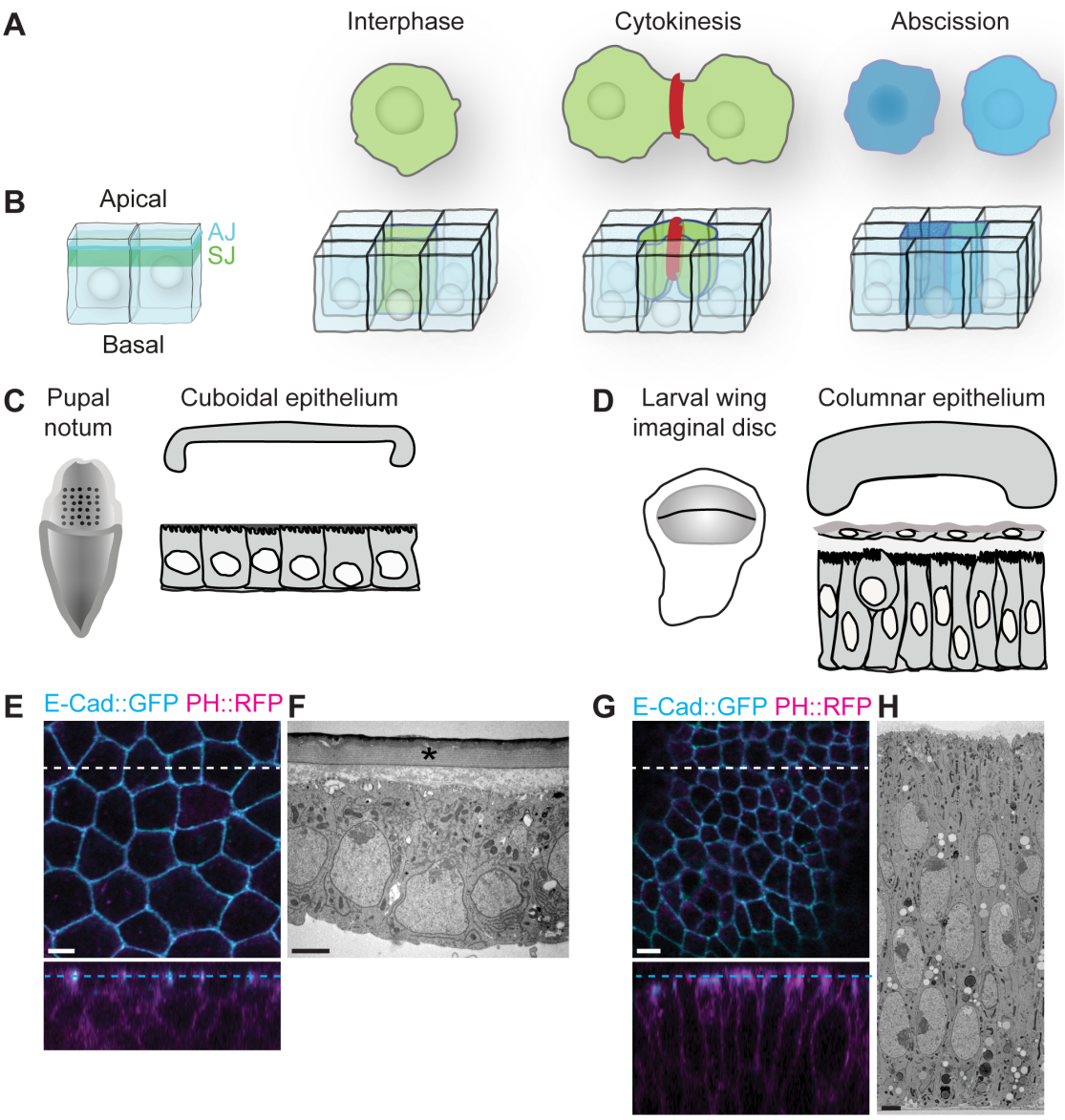

Figure S1. Model systems and methodology to study epithelial cytokinesis, related to Figure 1

(A-B) Schematic representations of cytokinesis in isolated (A) and epithelial cells (B). As they divide, epithelial cells remodel the AJ (blue) and SJ (green) cell-cell contacts.

(C-D) Schematic representations of the notum at pupal stage composed of cuboidal cells (C) and of the WID at larval stage made of columnar and squamous peripodial cells (D).

(E, G) Epithelial cells expressing the plasma membrane reporter PH::RFP (magenta) with E-Cad::GFP (cyan) in notum (E) or WID (G). Top views (top panels) or orthogonal sections (bottom panels, respective white dashed lines). Cyan dashed line highlights the level of AJ.

(F, H) TEM micrographs of dividing epithelial cells in notum (F) or WID (H) sectioned along the apico-basal axis. The asterisk labels the cuticle in F.

Scale bars represent 3 μm (E, G) or 2 μm (F, H).

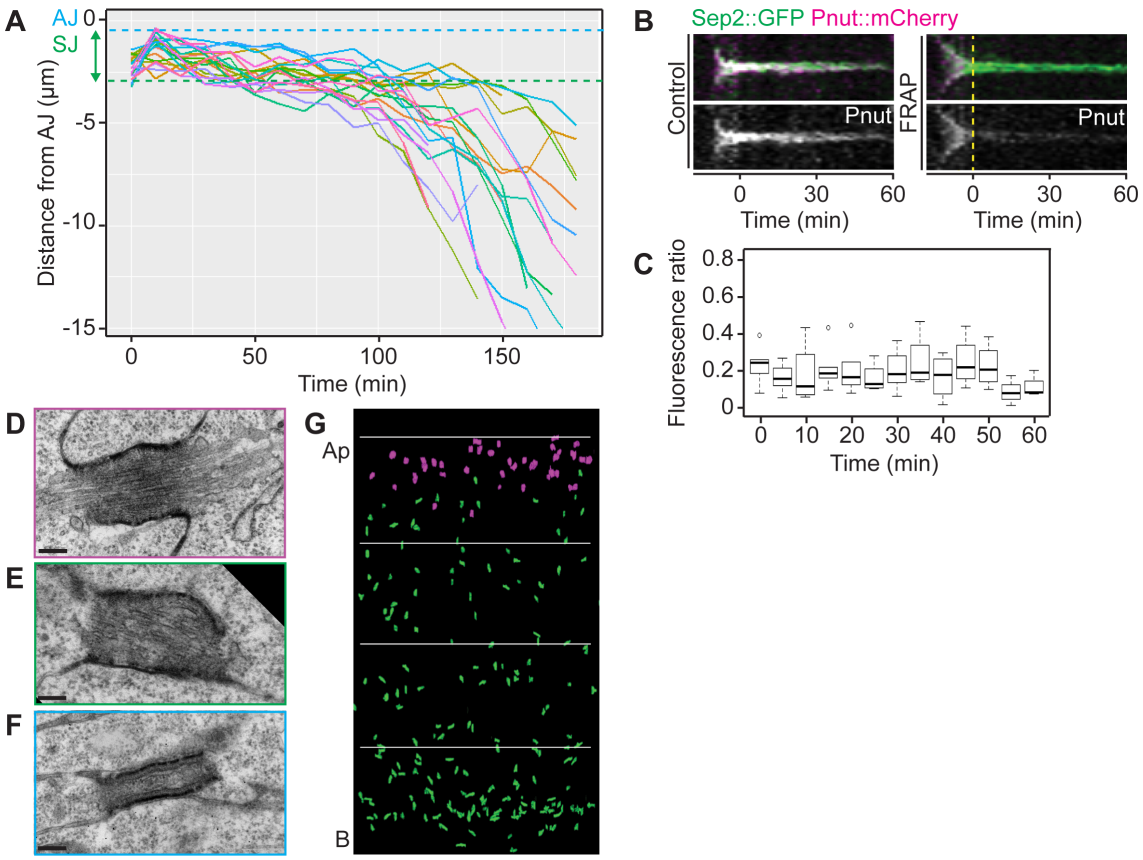

Figure S2. Midbody assembles and displaces toward the basal pole during cytokinesis, related to Figure 1

(A) Plot of the quantitation of the apical to basal movement of the midbody over time relative to AJ (cyan line: 0 to -0.5 μm) and SJ (green line: -0.5 to -3 μm). Each curve represents the displacement of a midbody from a single dividing cell (n=20).

(B) Kymographs of Pnut::mCherry (magenta) imaged with Sep2::GFP (green) present in the midbody over time in control condition (left panels) or upon photobleaching (right panels). Photobleaching of Pnut::mCherry was done 10 minutes following contractile ring constriction (yellow dashed line).

(C) Plot of the quantitation of the fluorescence signal recovery of Pnut::mCherry (n=5) after photobleaching over time.

(D-F) TEM micrographs of dividing WID epithelial cells sectioned parallel to the midbody. Three stages of midbody maturation are shown: the maturing midbody (D, magenta, n>20), the intermediate midbody (E, green, n>20) and the intercellular bridge (F, cyan, n>20).

(G) Maximal projection of orthogonal sections showing the distribution of maturating midbody (magenta) and intermediate midbody together with intercellular bridges (green) identified using the SFB-SEM volume reconstitution in WID.

Time is in minutes (A-C), with t=0 min corresponding to the onset of anaphase (A) or the time of photobleaching (B-C). Scale bars represent 200 nm.

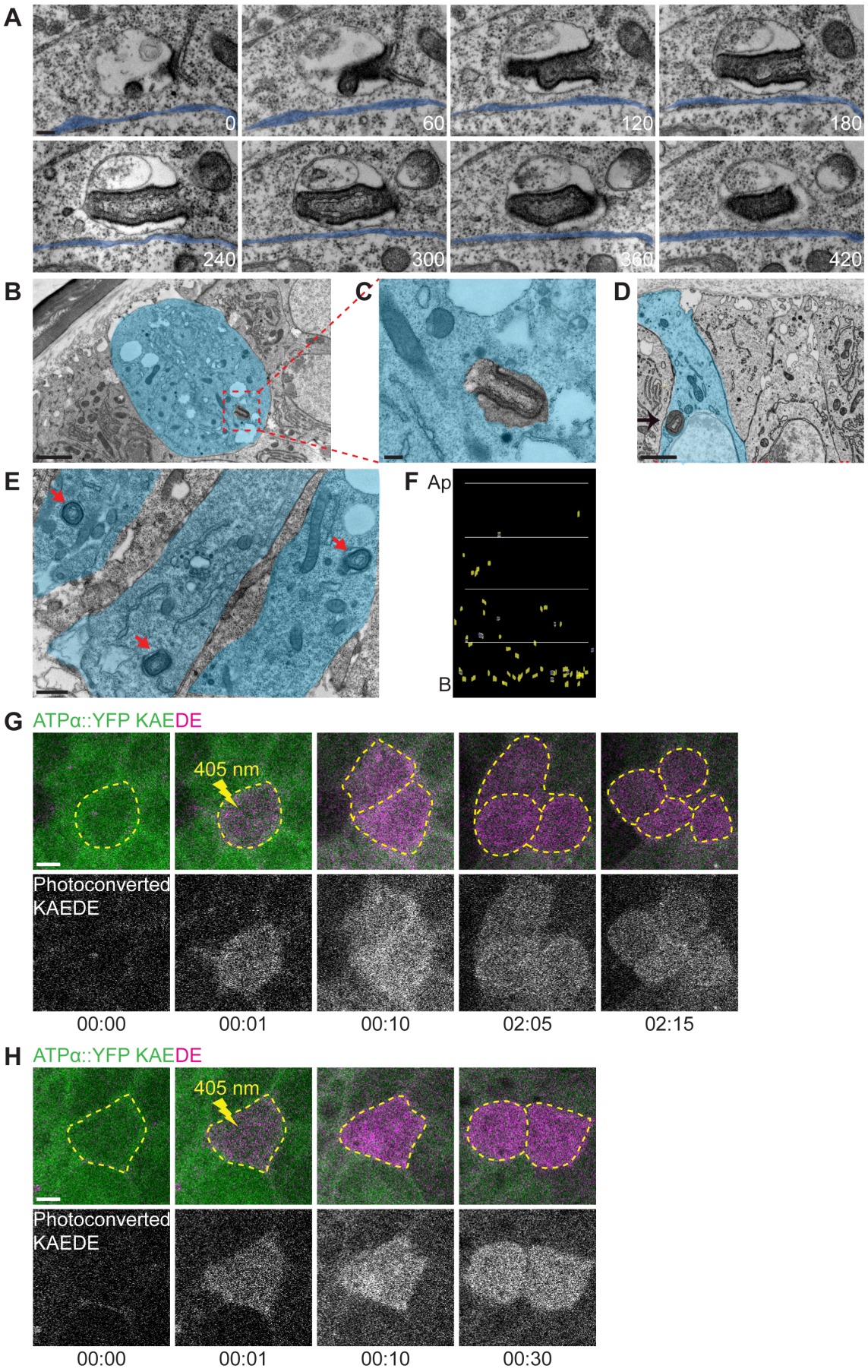
A
0
60
120
180
240
300
360
420
B
C
D
E
F
Ap
B
G
ATPα::YFP KAEDE
405 nm
Photoconverted KAEDE
00:00
00:01
00:10
02:05
02:15
H
ATPα::YFP KAEDE
405 nm
Photoconverted KAEDE
00:00
00:01
00:10
00:30

Figure S3. Abscission is temporally uncoupled to Shrb recruitment, related to Figure 2

(A) TEM micrographs of ultrathin serial sections of WID epithelial cells sectioned parallel to the intercellular bridge (n>20). Blue line labels the plasma membrane and numbers refer to the distance (nm) that separates the sections.

(B-E) TEM micrographs of epithelial cells sectioned parallel to degrading intercellular bridges in notum (B-D, n>20) or WID (E, n>20). The cytoplasm surrounding the degraded bridges is colored in cyan and red arrows show degrading bridges in E. C is a high magnification of the intercellular bridge depicted in the red inset in B.

(F) Maximal projection of orthogonal sections showing the distribution of intercellular bridges (yellow) and degrading bridges (blue) identified using the SFB-SEM volume reconstitution in WID.

(G-H) Time-lapse of dividing cells expressing ATPα::YFP (green) together with the photoconvertible probe KAEDE. Green to red (magenta) photoconversion of KAEDE was done (yellow lightning) in randomly chosen cells from pupae at 15h APF prior to it enters in mitosis. Yellow dashed line delineates the photoconverted dividing cell and its daughters. KAEDE did not diffuse to several cell diameters. Instead, photoconverted KAEDE was either diffusing and equilibrating with only one next neighbor (G, n=4 from 175 to 75 min) or was remaining restricted to the photoconverted cell (H). In the latter case, cells were entering mitosis shortly after photoconversion (H, n=5 from 70 to 5 min). Thus, this assay is faithfully reporting cytoplasmic isolation between the daughter cells.

Scale bars represent 3 μm (G-H), 2 μm (B-E) or 200 nm (A).

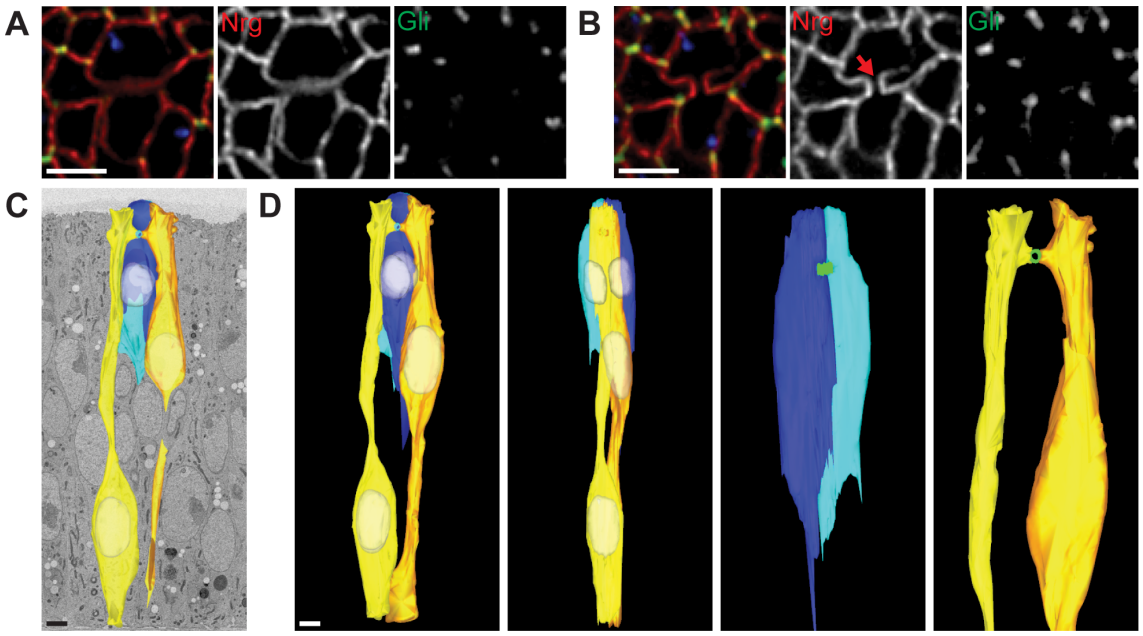

Figure S4. Dividing cells remain connected to their neighbors throughout cytokinesis, related to Figure 3

(A-B) WID epithelia expressing Nrg::GFP (red) and stained for Gli (green) and γ-tubulin (blue) at two focal planes (A is 0.6 μm apical to B). Red arrow points to the midbody.

(C-D) 3D model based on SFB-SEM dataset illustrating the membrane contact made between daughter cells (cyan and blue) and their neighbors (yellow and orange) in WID. Parallel or perpendicular views to the midbody (green) showing the daughters connected by the midbody and the neighbors that extend finger-like protrusions towards the midbody.

Scale bars represent 3 μm (A-B) or 2 μm (C-D).

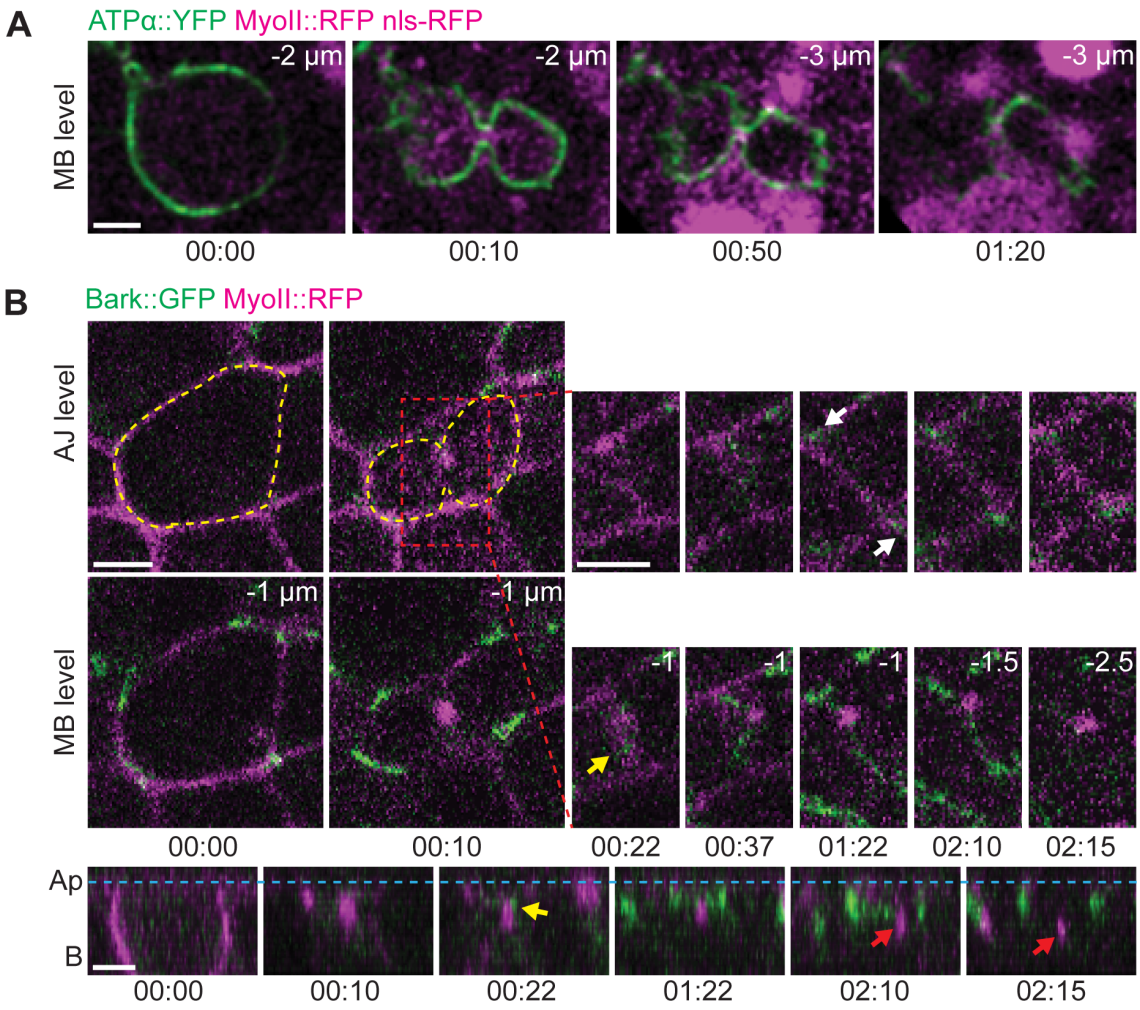

Figure S5. *de novo* assembly of SJ at the cleavage site , related to Figure 4

(A) Original data presented in the main Figure 4A. Time-lapse of a dividing cell expressing MyoII::RFP (magenta, with nls-RFP) with ATPα::YFP (green) (identified by the loss of nls-RFP) and surrounded by cells devoid of ATPα::YFP.

(B) Time-lapse of a dividing cell expressing MyoII::RFP (magenta) together with Bark::GFP (green) (n=8). High magnifications on right panels correspond to the inset (red lines) depicted at t=10 min. Yellow dashed line delineates the dividing cell and its neighbors, cyan dashed line highlights the position of AJ, red arrows point to the midbody, yellow arrows show the first Bark::GFP punctae and white arrows show the final Bark::GFP distribution at TSJ.

Time is in hour:minute, with t=0 min corresponding to anaphase onset. Distances (*µ*m) correspond to the position relative to the plane of AJ labeled with MyoII::RFP. Scale bars represent 3 µm.

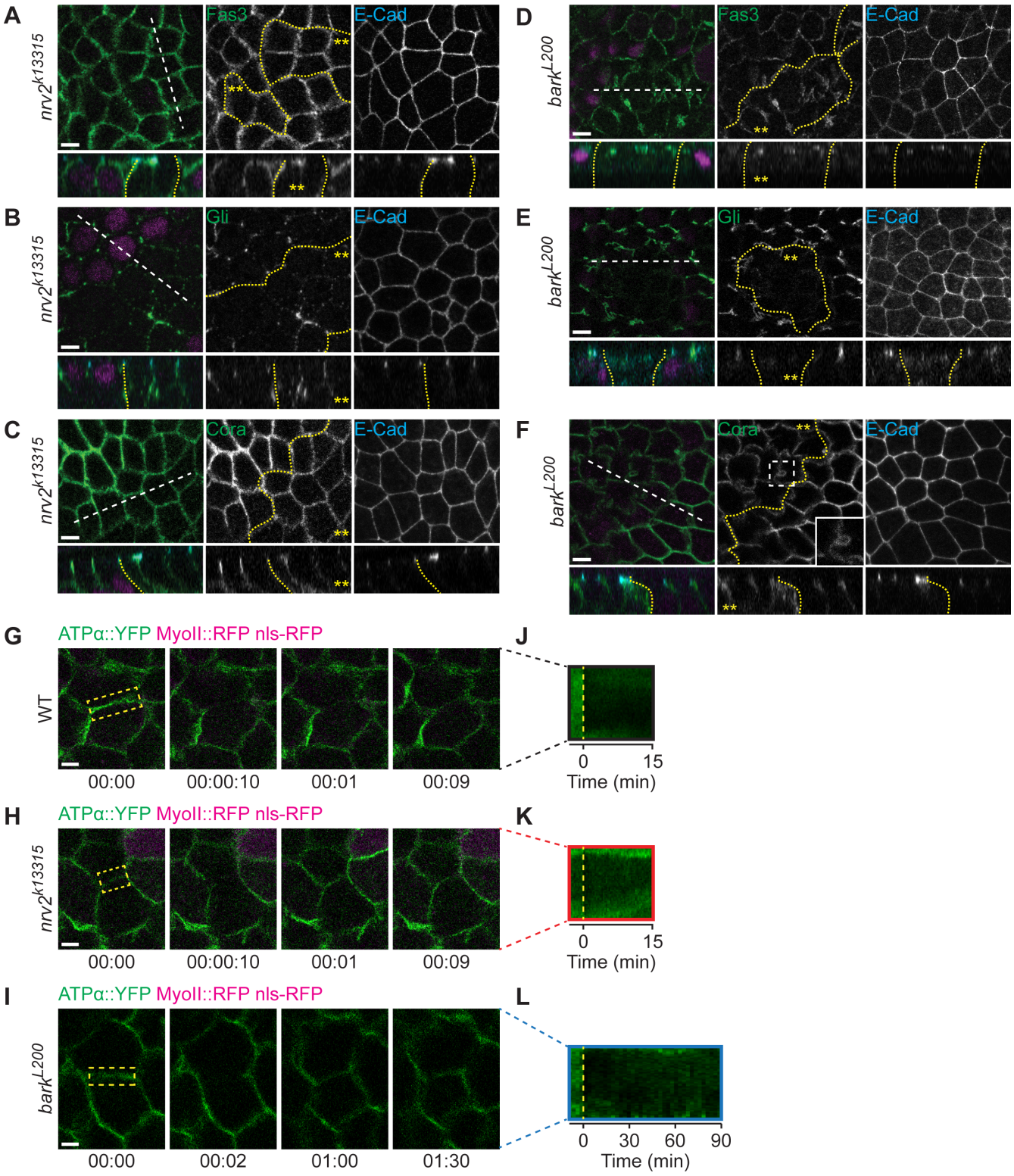

Figure S6. SJ components regulate midbody basal displacement, related to Figure 6

(A-F) *nrv2*^{k13315} (A-C) or *bark*^{L200} (D-F) mosaic tissue expressed E-Cad::GFP (cyan) and stained for Fas3 (green, A, n=7; D, n=12), Gli (green, B, n=7; E, n=8) or Cora (green, C, n=12; F, n=10). Top views (top panels) or orthogonal sections (bottom panels, respective white dashed lines). Yellow dashed lines delineate wild-type and mutant cells (yellow stars, identified by the loss of nls-RFP,

magenta). High magnification in F corresponding to the inset (white dashed lines) shows the Cora membrane deformations upon loss of Bark.

(G-I) Time-lapse of wild-type (G), *nrv2*^{k13315} mutant (H) or *bark*^{L200} mutant (I) interphase cells expressing MyoII::RFP (magenta, with nls-RFP) together with ATPα::YFP (green). The ROI depicted by the yellow dashed square was photobleached and analyzed for the following 15 (G-H) or 90 minutes (I). Top views 1 μm below AJ level.

(J-L) Kymographs representing the photobleaching of ATPα::YFP (green) and corresponding to wild-type (J), *nrv2*^{k13315} mutant (L) or *bark*^{L200} mutant (L) cells, depicted in G, H and I, respectively. Yellow dashed lines indicate the time of photobleaching.

Time is in hour:minute(:second) (G-I) or in minutes (J-L), with t=0 min corresponding to the time of photobleaching. Scale bars represent 3 µm.